Energy Conversion and Management 308 (2024) 118338

Contents lists available at ScienceDirect

Energy Conversion and Management

journal homepage: www.elsevier.com/locate/enconman

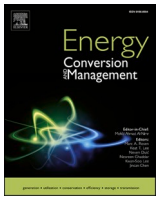

Optimal design of proton exchange membrane fuel cell systems for regional aircraft

Matthias Schröder *, Florian Becker, Christoph Gentner

German Aerospace Center (DLR), Institute of Engineering Thermodynamics, Hein-Saß-Weg 22, 21129 Hamburg, Germany

ARTICLE INFO

Keywords:
Fuel cell system
Cooling system
Pareto optimization
System performance
Aircraft propulsion

ABSTRACT

Proton exchange membrane fuel cells are considered to be a promising technology for future low-emission aircraft. However, the actual performance of fuel cell systems under aviation conditions is still unclear. To address this knowledge gap, this work develops a detailed model of a fuel cell system for the propulsion of a regional aircraft. The interaction of the stacks and auxiliary components is studied with validated models for the fuel cell stack, humidifier, heat exchanger and compressor. These models are coupled with a novel sizing approach that finds the smallest feasible combination of components while optimizing the stack operating conditions for each flight phase. Based on this approach, a wide range of possible fuel cell system designs is compared in terms of their mass, efficiency, drag and volume. The results show that it is beneficial to optimize these performance criteria simultaneously in a pareto optimization problem. The aircraft's electrical power demand of 3.12 MW is provided by ten identical 312 kW fuel cell systems that are distributed along the wing. Based on the model, such a 312 kW fuel cell system is predicted to achieve an efficiency of 39 % during cruise and 49 % on ground, a specific power of 0.50 kW/kg, a power density of 0.39 kW/L and a cruise drag of 333 N. Compared to conventional aircraft engines, fuel cells have the drawback of an increased mass and drag. The achievable propulsion system efficiency with fuel cells is lower than that of large turbofan engines, but higher than that of turboprop engines for regional aircraft.

1. Introduction

Without major emission reductions, commercial aviation could account for a significant share of human-induced global warming by the year 2050 [1]. The aviation industry is therefore exploring innovative propulsion technologies that go beyond incremental improvements to the kerosene consumption of conventional engines. One of the investigated approaches is to use hydrogen as an alternative energy source for passenger aircraft [2]. If the hydrogen is produced from renewable sources, this could, in the long term, eliminate in-flight carbon emissions from aviation.

In currently investigated concepts, hydrogen is either burned in modified gas turbine engines or used to generate electric power with fuel cells [3,4]. The electric power is then used to drive propellers via electric motors [5] or is provided to auxiliary loads onboard the aircraft [6]. For the propulsion of mid- and long-range aircraft, hydrogen combustion is generally viewed as superior to fuel cells because of the higher specific power of large gas turbines [2]. For the propulsion of smaller aircraft, low-temperature proton exchange membrane fuel cells (PEMFC) are a promising alternative because of their higher efficiency at lower power requirements and non-existent nitrogen oxide emissions [3,7]. This work investigates the case where fuel cells provide propulsive power for a 70 passenger regional aircraft.

There is still a significant uncertainty regarding the feasibility of PEMFCs for aircraft propulsion. Nearly a decade ago, Epstein [8] concluded that fuel cells were unlikely to become a suitable option for the propulsion of commercial aircraft. More recently, Massaro et al. [3] showed that fuel cells could indeed be suitable for the hybrid-electric propulsion of regional aircraft. Smith et al. [9] came to the more optimistic conclusion that fuel cell propulsion could even become viable for long-range aircraft by the year 2050. These substantially different results show that there is a knowledge gap regarding the actual performance of fuel cell systems under aviation conditions. This work seeks to address this knowledge gap by providing accurate predictions for the currently achievable fuel cell system performance under such conditions. The main performance criteria for aircraft propulsion technologies are their technical performance, safety and reliability, environmental impact and cost [8,10]. Here, we focus on the technical performance in terms of mass, efficiency, aerodynamic drag and volume.

* Corresponding author.
E-mail address: matthias.schroeder@dlr.de (M. Schröder).

https://doi.org/10.1016/j.enconman.2024.118338
Received 9 January 2024; Received in revised form 26 February 2024; Accepted 20 March 2024
Available online 15 April 2024

Nomenclature

Symbol	Description
A	Area (m^2)
a	Area, normalized with heat flow (m^2/W)
ADT_{hm}	Humidifier approach dew point temperature (°C)
b	Bypass ratio (-)
C	Heat exchanger stream capacity rate ($J\,K^{-1}s^{-1}$)
c	Fluid velocity (m/s)
c_p	Specific heat capacity ($J\,kg^{-1}K^{-1}$)
d_h	Hydraulic diameter (m)
F	Faraday constant $(A\,s\,mol^{-1})$
F_d	Drag force (N)
f_{fric}	Fanning friction factor (-)
h	Specific enthalpy (J/kg)
i	Current density (A/m^2)
k	Coefficients in correlations
l	Length (m)
L	Flow length of heat exchanger (m)
m	Mass (kg)
$\dot{m}$	Mass flow (kg/s)
n_{cp}	Rotational speed of compressor shaft (1/s)
n	Amount of substance (mol)
$\dot{n}$	Molar flow (mol/s)
N	Number of components (-)
Nu	Nusselt number (-)
Ntu	Heat exchanger: number of transfer units (-)
p	Pressure (Pa)
P	Electrical power (W)
$\dot{Q}$	Heat flow (W)
R	Universal gas constant ($J\,K^{-1}mol^{-1}$)
R_{sp}	Specific gas constant ($J\,kg^{-1}\,K^{-1}$)
Re	Reynolds number (-)
RH	Relative humidity (-)
T	Temperature (K, °C)
U_{cell}	Cell voltage (V)
$uA_{s,eff}$	Heat transfer conductance (W/K)
V	Volume (m^3)
$\dot{V}$	Volume flow (m^3/s)
X	Molar fraction (-)

Greek symbols

α	Heat transfer coefficient ($W\,m^{-2}\,K^{-1}$)
δ	Thickness (m)
ε_{hx}	Heat exchanger effectiveness (-)
η	Efficiency (-)
η_c, η_Ω, η_m	Voltage losses (V)
λ	thermal conductivity $(W\,m^{-1}\,K^{-1})$
λ_{O_2}	Cathode stoichiometric ratio (-)
λ_{H_2}	Anode stoichiometric ratio (-)
μ	Dynamic viscosity ($kg\ m^{-1}\,s^{-1}$)
Π	Pressure ratio of compressor (-)
ρ	Density (kg/m^3)
σ	Membrane permeability ($mol\,s\,kg^{-1}$)

Subscripts

A	anode side of cells in stack
ac	air cooler and related systems
ar	anode recirculation blower
base	baseline
C	cathode side of cells in stack
c	cold side of heat exchanger
cell	cell, cell-level quantity
cp	compressor
cr	cross-section
cw	coolant
dr	diffuser
dew	dew point
des	design point
eff	effective
ep	end-plate (of stack)
FC	fuel cell stack and related systems
front	frontal area of heat exchanger
h	hot side of heat exchanger
hm	humidifier
hm,d	dry side of humidifier
hm,w	wet side of humidifier
hx	heat exchanger
in	inlet
max	maximum
mix	mixed
mem	membrane
norm	normalized
nz	nozzle
out	outlet
pu	coolant pump
react	reactant air and related systems
red	reduced
ref	reference
req	required
sat	saturation
stack	stack
sys	system-level quantity
tot	total

In the context of aircraft applications, the size of each fuel cell system component will likely be optimized instead of relying on existing off-the-shelf components. Hence, the assessment methodology needs to be flexible enough to consider varying component sizes. At the preliminary design stage, such fuel cell systems are therefore commonly studied with scaled steady-state models [7,10,11]. After assessing a wide range of possible designs, a specific design can be studied in more detail with transient simulations [12] and experiments with full-scale prototypes [5]. This work develops a model that enables an accurate prediction of the steady-state system performance during the preliminary design stage.

Previous studies on PEMFC systems for aircraft applications have assessed various aspects of the system performance. Sparano et al. [11] developed a preliminary design methodology for a MW-scale hybrid PEM fuel cell/battery propulsion unit in regional aircraft and investigated the coupled effects of the energy management and degree of hybridization. Abu Kasim et al. [7] designed a PEMFC system for an 8 passenger aircraft based on lumped models for the stack and auxiliary components. The developed model was used to assess the steady-state performance of the envisioned aircraft. Park et al. [13] investigated an electric vertical take-off and landing aircraft and sized the fuel cell system, hydrogen tank and battery system for different scenarios. Focusing on a large MW-scale PEMFC system, Kösters et al. [10] compared a conventional liquid-cooling concept to a phase-change-heat-pump cooling concept. Vietze and Weiland [14] conducted a transient analysis for a 500 kW fuel cell powertrain. Their analysis

showed that hydrogen evaporation and supply can be achieved passively, i.e. without electric heaters or hydrogen pumps. A recent study by Li et al. [15] investigated the optimal cathode pressure for an aircraft fuel cell powertrain based on semi-empirical models for a fuel cell stack and air compressor. Lüdders et al. [16] developed a design method for fuel cell auxiliary power units and derived a pareto front with respect to the system's mass and efficiency.

These previous studies have in common that they use lumped (zero-dimensional) component models. The use of such simplified models is an effective way to reduce the model complexity and computational cost at the preliminary design stage. However, this limits the accuracy of the predicted system performance as several relevant effects cannot be captured: In previous design approaches, the stacks are often assumed to operate at a constant pressure independent of the flight altitude and ambient pressure [7,10,11,13,14,16]. This results in a non-optimal usage of the compressor and reduces the system efficiency [15,17]. Moreover, the compressor's limited operating range and variable efficiency are often not considered [10,13,14], but were shown to significantly affect the range of feasible stack operating conditions [15]. Another common simplification is to neglect the effect of a non-ideal humidification of the reactant air [10,13,14,16]. However, this effect should be considered because it can have a significant impact on the stack's efficiency [12]. Another limitation of previous approaches is that they optimize only one or two design targets at a time. For example, ref. [7] optimized the system efficiency, ref. [16] the system efficiency and mass, ref. [10] the aerodynamic and mass-induced drag, ref. [13] the payload and ref. [14] the mass of the fuel cell system and tank. The remaining technical performance aspects are determined implicitly or not at all. In some cases, this may give an incomplete impression of the system's overall technical performance.

This work presents a novel sizing approach for aircraft fuel cell systems that overcomes the above limitations:

1. A PEMFC system for aircraft applications is studied with detailed and validated component models. The developed system model captures the relevant component-level effects and yet remains flexible enough to consider varying component sizes. The modeling approach enables more accurate results, because the limited operating range and variable efficiency of the compressor and humidifier can be considered in detail. The system model is coupled with a sizing algorithm that finds the smallest feasible combination of components while optimizing the stack operating conditions for each flight phase. This leads to more reliable predictions for the system performance, because the components can be sized to match their specific requirements while maintaining a detailed modeling approach.
2. It is shown that it is possible and beneficial to consider the design of PEMFC systems as a pareto (multi-objective) optimization problem. The proposed approach considers different design targets such as a low mass, high efficiency, low drag and low volume simultaneously. This leads to system designs that perform well for all of these contradicting design targets. The pareto-optimal system is shown to perform better than designs that focus on a single design target.

The proposed approach enables a comprehensive assessment of the performance of fuel cell systems for regional aircraft propulsion. A detailed mass breakdown of the fuel cell system is derived and identifies the components that have the largest impact on the overall system performance. The pareto-optimal design approach is applied to an exemplary 312 kW system for a regional aircraft. Because the approach is based on scalable component models, it can also be used for other applications of fuel cell systems with a power output of up to several hundred kW.

2. System description

The fuel cell system is designed for a 70 passenger regional aircraft design by Atanasov [18], which is comparable in size to an existing ATR 72–600 aircraft [19]. The investigated aircraft is designed as a distributed propulsion concept [20] where thrust is provided by multiple propulsion units that are distributed along the wing (see Fig. 1 (a)). Each of the ten propulsion units contains a 312 kW fuel cell system and a small battery that assists during takeoff (see Fig. 1 (b)). This work focusses on the design of the fuel cell system. The battery storage, power converters and electric grid provide boundary conditions to the model and are not investigated in detail. The aircraft operates at an altitude of 8840 m and a cruise velocity of Mach 0.55; the mission profile is discussed in section 5.2.

Fig. 1 (c) shows the chosen layout of the fuel cell system in one of the ten propulsion units. The power output of one fuel cell stack is typically limited to about 125 kW [21]. Future stack designs may achieve higher power outputs per stack, but this study focusses on technology that exists today. Hence, several identical stacks are combined to achieve the required net power output of 312 kW. This modular approach has the benefit of increasing the system's redundancy if one of the stacks fails during flight. The figure shows an exemplary case with 2 stacks; the actual required number of stacks is a result of the sizing process. Each stack is connected to a membrane humidifier and an anode recirculation loop. Because compressors and heat exchangers can be scaled to larger power outputs, the air supply and cooling system are designed to provide the required fluid flows for all stacks combined.

The air supply system begins with a diffuser that reduces the velocity of the incoming air. A single-stage radial compressor then raises the air pressure from ambient conditions (as low as 0.31 bar during cruise) to the desired amount at the stack's cathode inlet ($\geq$1 bar abs.). The compressor is driven by an electric motor that is powered by the fuel cell stacks. Such electrically driven compressors are a mature technology in aircraft and are for example used in the electric environmental control system of the Boeing 787 [22].

The pressure ratio of a single-stage radial compressor is typically limited to 3.5 to 4.5 [23,24]. Therefore, the stack pressure is adjusted depending on the flight altitude in order to keep the compressor's pressure ratio below this limit (see section 4). In principle, a two-stage compressor could be used to achieve higher stack pressures at the cruise altitude. However, to the knowledge of the authors there is no existing two-stage compressor described in the public literature that can provide the required mass flow of up to 0.8 kg/s. On the other hand, single-stage compressors of the required size are commonly used for automotive supercharger/turbocharger applications [25]. Therefore, a single-stage compressor is considered by the model. Automotive radial turbo-compressors might have minor design differences compared to aircraft radial turbo-compressors. Their normalized operating maps nevertheless provide a reasonably accurate data source for the preliminary sizing approach that is developed in this work.

Another potential performance improvement could be achieved by coupling the compressor shaft to a turbine that expands the stack's cathode exhaust [7,23]. However, this would require an intricate design strategy to match the turbine's narrow operating range to the wide range of pressure ratios and mass flows that occur throughout the flight mission. A feasible design may be achieved with a variable-geometry turbine [26]. However, this would increase the system's complexity, require mechanical actuators and thereby add potential failure modes. The model therefore considers a more conservative design without a turbine.

After the compressor, an air-to-air heat exchanger is used to cool the compressed air to a tolerable temperature (85 °C) at the humidifier inlet. Next, the air is humidified with the stack's cathode exhaust stream. The liquid phase of the cathode exhaust stream is removed in a water separator before entering the wet side inlet of the humidifier. The hydrogen is stored in liquid form in the rear of the aircraft and is evaporated before being supplied to the fuel cell system. It is considered to be present in gaseous form at the required pressure and temperature at the system boundary of the investigated propulsion unit. The cooling

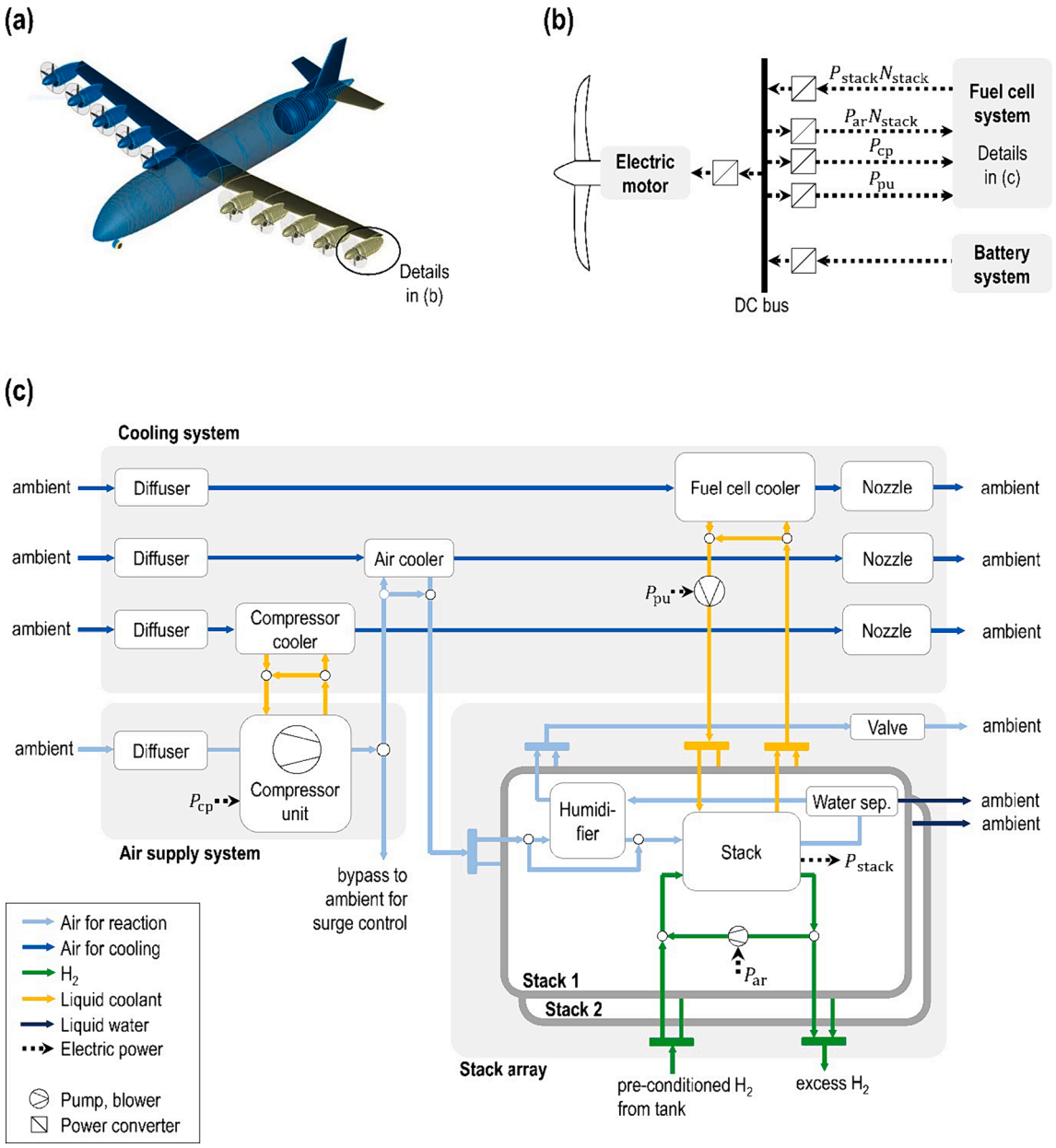

Fig. 1. Fuel cell system for regional aircraft. (a) Aircraft concept by Atanasov [18], image reproduced with permission, (b) electric layout for one of the ten propulsion units, (c) fuel cell system in one of the ten propulsion units.

system contains three heat exchangers to remove the stacks' waste heat and to cool the compressed air and the compressor itself. Diffusers are used to convert the kinetic energy of the cooling air streams to an increased static pressure. After the heat exchangers, variable-area nozzles convert the excess static pressure to an increased exit velocity in order to decrease the drag. The cooling system is designed to be passive, i.e. it is operated without an additional fan during flight. This is possible if the cold side pressure drop of the respective heat exchanger is lower than the pressure increase in the diffuser. In the investigated aircraft concept, the cooling system is designed to work when the air enters the diffusers with a velocity of $\geq$ 70 m/s [18]. This velocity is reached several seconds after takeoff. Before this velocity is reached, the aircraft uses power from the battery storage (see Fig. 1 (b)) and the stacks are kept in idle mode.

2.1. System performance indicators

The system's effective power output $P_{sys,eff}$ is given by

$$P_{sys,eff} = N_{stack}(P_{stack} - P_{ar}) - P_{cp} - P_{pu} \quad (1)$$

where N_{stack} is the number of stacks and P is the power flow to or from the respective component as defined in Table 1. The system's overall efficiency is defined as

$$\eta_{sys,LHV} = \frac{P_{sys,eff}}{\dot{m}_{H_2,sys}\Delta h_{LHV,H_2}} \quad (2)$$

where $\dot{m}_{H_2,sys}$ is the mass flow of hydrogen to the stacks and $\Delta h_{LHV,H_2}$ is the lower heating value (LHV).

The mass of the fuel cell system $m_{sys} = \sum m_i$ is estimated with the most relevant components, which are listed in Table 1. The overall mass m^*_{sys} is increased by a constant term m_{offset} that accounts for the

Table 1
Overview on the fuel cell system components that are included in the model.

Component	Power flow	Mass	Volume	Modeling approach
Stack	P_{stack}	m_{stack}	V_{stack}	1D, two-phase
Humidifier	–	m_{hm}	V_{hm}	1 + 1D, single-phase
Fuel cell cooler	–	$m_{hx,FC}$	$V_{hx,FC}$	1D, single-phase
Air cooler	–	$m_{hx,ac}$	$V_{hx,ac}$	1D, single-phase
Compressor cooler	–	$m_{hx,cp}$	$V_{hx,cp}$	1D, single-phase
Compressor unit	P_{cp}	m_{cp}	V_{cp}	0D, variable efficiency
Stack coolant pump	P_{pu}	m_{pu}	V_{pu}	0D, constant efficiency
Anode recirculation blower	P_{ar}	m_{ar}	V_{ar}	0D, constant efficiency
Diffusers and nozzles	–	–	–	0D, constant efficiency

additional mass of structural components, pipes, valves and electrical connections as well as the mass of the diffusers and nozzles.

$$m^{*}_{sys} = m_{sys} + m_{offset} \tag{3}$$

The underlying assumption is that m_{offset} remains nearly constant for different design choices and that it is sufficient to minimize m_{sys} in order to find the optimal system design. Following refs. [12,27], the hydrogen tank and supply system are treated as separate systems and are not included in the fuel cell system mass. The design of a liquid hydrogen tank and supply system is a complex problem in its own right [14,28] and is beyond the scope of this work. The system's volume is defined as

$$V^{*}_{sys} = V_{sys} + V_{offset} \tag{4}$$

with the components in Table 1. Analogously to the mass, the calculated volume V_{sys} does not account for the additional volume of structural components, pipes, valves and electrical connections as well as the volume of the diffusers and nozzles.

The overall aerodynamic drag of the fuel cell system is the sum of its internal drag, external drag and weight-induced drag [10]. The internal drag is caused by the deceleration of the cooling air streams. It is given by

$$F_{d} = \dot{m}_{dr}(c_{dr,in} - c_{nz,out}) \tag{5}$$

where $c_{dr,in}$ and $c_{nz,out}$ are the velocities at the inlet of the diffuser and the exit of the nozzle and $\dot{m}_{dr}$ is the respective air mass flow. The additional drag that is caused by the reactant air stream $F_{d,react}$ is calculated under the conservative assumption that this air stream cannot be accelerated in a nozzle after passing through the stack's pressure regulating valve.

$$F_{d,react} = \dot{m}_{cp} c_{dr,in} \tag{6}$$

The total internal drag is

$$F_{d,tot} = F_{d,FC} + F_{d,ac} + F_{d,cp} + F_{d,react} \tag{7}$$

where F_{d} is calculated for the stack cooling loop (subscript "FC"), air cooling loop (subscript "ac") and compressor cooling loop (subscript "cp"). Calculating the external and weight-induced drag with a similar degree of detail would require a detailed assessment of the overall aircraft aerodynamics. Therefore, the internal drag is used in this work to compare different fuel cell system designs to one another.

3. Mathematical model development

The fuel cell system model consists of a number of component models that are coupled via fluid and power flows. It aims to capture sizing-relevant phenomena while still maintaining a sufficiently low computational cost for assessing a large number of possible designs. The degree of detail for each component model is therefore chosen based on its significance to the overall system performance (see Table 1). The models and accompanying sizing algorithms are implemented in MATLAB. Fluid properties are considered with data from ref. [29] for humid air and ref. [30] for the liquid coolant. The liquid coolant is a 50 % (volume/volume) mixture of water and ethylene glycol. Throughout the component models, the following assumptions are made:

- Ideal gases and incompressible liquids
- Constant specific heat capacity $c_{p}(T)$, evaluated at the inlet or outlet temperature of the respective component (except in the compressor model)
- Humid air is modelled as an ideal gas mixture of oxygen, nitrogen and water vapor (except in the two-phase stack model)

The ideal gas assumption is valid, because the modelled fluids are present at moderate temperatures (-45 °C to < 200 °C) and low pressures (<3 bar) [31]. The assumption of a constant specific heat capacity c_{p} also provides sufficiently accurate results: Within the heat exchangers, the liquid coolant temperature changes by < 15 °C and the air temperature changes by < 100 °C. Within this temperature range, the c_{p} of these fluids varies by < 2 % [29,30]. In the case of the compressor, the air temperature changes by more than 100 °C and the temperature dependence $c_{p}(T)$ is considered explicitly (see section 3.4).

In agreement with previous studies, steady-state models are used for the preliminary design of the system and the mission profile is approximated with a number of steady-state operating points [7,10,11,13,14,16]. Changes of the ambient pressure and temperature at different altitudes are considered with the international standard atmosphere (ISA) [32]. An offset of $\Delta T = 22.8$ °C is added to the ISA temperature profile to account for a "hot day" scenario when sizing the cooling system. This results in an ambient temperature of 37.8 °C at sea level [33]. The "hot day" scenario is selected because it is the worst-case ambient condition for the investigated system: A larger heat exchanger is required if the temperature difference between the cold fluid (ambient air) and the hot fluid (stack coolant) is small. Moreover, the compressor requires slightly more power for higher air temperatures (see Eq. (47) in section 3.4).

3.1. Fuel cell stack

The stack is modelled based on a 1D, two-phase model for low-temperature PEMFC stacks that is explained in detail in an earlier publication [17]. Briefly summarized, the model is based on a 1D discretization perpendicular to the membrane surface area and is designed to capture water management effects in a computationally efficient way. The model uses the common approach of simulating the performance of a stack by simulating an averaged cell of the stack [34]. The original model version in ref. [17] was developed for a Hydrogenics HD4 stack. For the purpose of this work, the model was re-parameterized with new experimental data for a Powercell S3 stack. This stack type achieves a stack-level specific power of up to 3 kW/kg and a power output of up to 125 kW when it is scaled to the maximum number of cells [21]. This makes it a promising baseline for the stacks that may one day be used in commercial aircraft. The following subsections describe how the stack model is re-parameterized, extended and integrated into the overall system model. The model's input and output variables are summarized in Appendix A, Table A.1.

3.1.1. Experimental data

A 20-cell version of a Powercell S3 stack with a rated power output of 5.5 kW was characterized under steady-state galvanostatic operation. The measurements were conducted on a custom stack test bench that is described in refs. [17,35]. Since the time of these publications, the test

bench was extended with a Fumatech H10N membrane humidifier which uses the stack's cathode exhaust as the wet-side fluid (in counterflow operation). The humidity at the stack's cathode inlet is controlled by partially bypassing the humidifier's dry side with a three-way valve. The stack's cell voltages as well as a number of temperatures, pressures and mass flows are measured for varying current densities, cathode inlet pressures, stoichiometric ratios and temperatures. The stacks are operated with the same anode recirculation concept that is described in ref. [17]. The results of the measurements are discussed in section 5.1.1.

3.1.2. Model parameterization

The stack model depends on several known parameters (such as active cell area A_{cell}, number of cells N_{cell}) and several fitted parameters. The fitted parameters are listed in Appendix A, Table A.2. These parameters were fitted to the experimental data of a Powercell S3 stack (see section 3.1.1). The 52 steady-state operating points that were used to fit the model parameters are discussed in section 5.1.1. The difference between the measured and simulated cell voltage is minimized with MATLAB's genetic optimization algorithm, using the approach that is described in ref. [17]. All fitted parameters are constrained to a plausible range, the bounds that were used when fitting these parameters are given in Appendix A, Table A.2. The model's governing equations are kept the same as in ref. [17], except for two minor modifications. The first modification is that the conductivity of Nafion is now determined based on the more commonly used correlation by Weber and Newman [36–38]. Secondly, the empirical correlation for the stack's cathode side pressure drop was replaced by Eq. (8) in order to better match the pressure drop characteristic of the new stack.

$$\Delta p_{stack,C} = k_{pC} \frac{\dot{m}_{stack,C,in}}{N_{cell}} \tag{8}$$

The parameter k_{pC} is fitted to the measured cathode side pressure drop of the Powercell S3 stack at different air mass flows. Because Eq. (8) uses the air mass flow per cell, it is also applicable for a different number of cells in a stack.

3.1.3. Integration into the overall system model

In order to determine the stack's waste heat, the model from ref. [17] is extended with a heat balance (see Appendix A). When sizing the overall system, the stack's cell voltage is evaluated for a given current density i_{des} at the system's design point. The required total number of cells in the system is determined based on the stack's power output per cell.

$$P_{cell} = A_{cell} i_{des} U_{cell} \tag{9}$$

$$N_{cell,tot} = \frac{N_{stack} P_{stack}}{P_{cell}} \tag{10}$$

This number is then divided among the minimum number of equal-sized stacks that do not exceed the maximum limit $N_{cell,max} = 455$ for the number of cells per stack [21].

$$N_{stack} = \text{ceil}\left(N_{cell,tot}/N_{cell,max}\right) \tag{11}$$

$$N_{cell} = \text{ceil}\left(N_{cell,tot}/N_{stack}\right) \tag{12}$$

This approach makes use of the fact that the stack's simulated power output and pressure drop correlations scale linearly with the number of cells. The stack's mass and volume are given by

$$m_{stack} = m_{cell} N_{cell} + m_{stack,ep} \tag{13}$$

$$V_{stack} = V_{cell} N_{cell} + V_{stack,ep} \tag{14}$$

where the parameters $m_{cell} = 0.072$ kg, $m_{stack,ep}$=9.139 kg, V_{cell}=0.068 L and $V_{stack,ep} = 7.143$ L were derived from ref. [21]. The parameters m_{cell} and V_{cell} account for an individual cell, the parameters $m_{stack,ep}$ and $V_{stack,ep}$ account for the two endplates in each stack. The consumed hydrogen flow per stack is

$$\dot{m}_{H_2,stack} = \frac{i A_{cell} M_{H_2} \lambda_{H_2} N_{cell}}{2F} \tag{15}$$

where i is the current density, M_{H_2} the molar mass of hydrogen, F the Faraday constant and $\lambda_{H_2} = 1.05$ the overall anode stoichiometric ratio (based on the hydrogen flow that is added to the recirculation loop).

3.2. Humidifier

The model considers a membrane humidifier with a cubic core geometry based on the Fumatech Ecomate series [39]. The dry air that needs to be humidified flows inside several hundred small tubes. The outer wet air stream flows in the opposite direction (see Fig. 2 (a)).

3.2.1. Humidification performance

The humidification performance can be expressed in terms of the approach dew point temperature [40]

$$ADT_{hm} = T_{dew,w,in} - T_{dew,d,out} \tag{16}$$

where the dew point temperature $T_{dew}(p_{H2O})$ depends on the partial pressure of water vapor p_{H2O}. The partial pressure of water vapor is

$$p_{H2O} = RH_{hm} p_{sat} \tag{17}$$

where $p_{sat}(T)$ is the equilibrium water vapor pressure [41] at the respective location. The relative humidity at the humidifier's wet side inlet is determined by the stack model. The dry side inlet humidity is set as $RH_{hm,d,in} = 0$. This ambient condition represents the worst-case scenario when sizing the humidifier, because it requires the largest amount of water to be added to the stream of hot compressed air. The relative

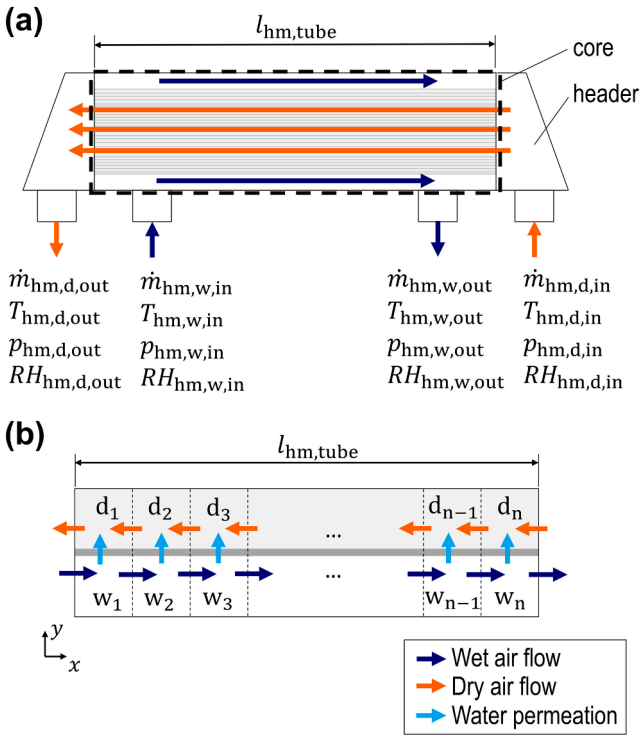

Fig. 2. Modelling domain of the humidifier model. (a) Mass flows in the investigated shell-and-tube humidifier (b) Spatial discretization of control volumes for the core (dry side control volumes are labelled as $d_1, \ldots, d_n$, wet side control volumes as $w_1, \ldots, w_n$).

humidity at the dry and wet side outlet is determined by solving a mass balance for discretized control volumes that are defined below.

The humidifier's total volume consists of the core and header volumes (see Fig. 2 (a)).

$$V_{\mathrm{hm}} = V_{\mathrm{hm,core}} + V_{\mathrm{hm,head}} \tag{18}$$

To consider the complex internal geometry of the core in a computationally efficient way, the inner volume of all tubes is represented by a single large volume $V_{\mathrm{hm,d}}$. The volume that is occupied by the wet fluid $V_{\mathrm{hm,w}}$ is represented by a second volume that is in contact with $V_{\mathrm{hm,d}}$ via the surface area A_{mem} of all tubes combined (see Fig. 2 (b)). That area is given by

$$A_{\mathrm{mem}} = N_{\mathrm{hm,tube}} l_{\mathrm{hm,tube}} \pi d_{\mathrm{hm,tube}} \tag{19}$$

where $d_{\mathrm{hm,tube}}$ and $l_{\mathrm{hm,tube}}$ are the mean diameter and length of a tube and $N_{\mathrm{hm,tube}}$ is the number of tubes. The volumes are

$$V_{\mathrm{hm,core}} = V_{\mathrm{hm,w}} + V_{\mathrm{hm,d}} \tag{20}$$

$$V_{\mathrm{hm,d}} = N_{\mathrm{hm,tube}} \pi \left(\frac{d_{\mathrm{hm,tube}}}{2}\right)^2 l_{\mathrm{hm,tube}} \tag{21}$$

$$V_{\mathrm{hm,w}} = r_{\mathrm{hm,V}} V_{\mathrm{hm,d}} \tag{22}$$

The volume of the tube's wall material is neglected because the tube wall thickness $\delta_{\mathrm{hm,tube}}$ is much smaller than the tube diameter. The outer volume $V_{\mathrm{hm,w}}$ is determined by scaling the inner volume $V_{\mathrm{hm,d}}$ with a fitted factor $r_{\mathrm{hm,V}}$ (see section 3.2.3).

To account for the variation of relative humidity along the flow length, $V_{\mathrm{hm,w}}$ and $V_{\mathrm{hm,d}}$ are each discretized into $n = 25$ control volumes (see Fig. 2 (b)). The model assumes that in-plane water transport in the membrane has a negligible effect on the overall humidification performance. This results in a 1 + 1D discretized model where water is transported via:

- forced convection in the wet and dry air streams along the flow length (x-axis in Fig. 2 (b))
- permeation across the membrane perpendicular to the flow length (y-axis in Fig. 2 (b))

The forced convection along the flow length is a result of the air flow that is imposed by the compressor. The molar flows $\dot{n}_{\mathrm{hm,d,in}}$ and $\dot{n}_{\mathrm{hm,w,in}}$ that enter the first control volume at the dry and wet side (elements w_1 and d_n in Fig. 2 (b)) are model inputs. The molar flows between the following control volumes are calculated with a mass balance as described below. The driving force for the permeation of water across the membrane is a difference in partial pressure of water vapor on the dry and wet side. The permeation process includes the absorption of water vapor by the membrane, the diffusion through the membrane and the desorption on the opposite side of the membrane [42]. It holds

$$J = \frac{\sigma_{\mathrm{mem}}}{\delta_{\mathrm{hm,tube}}} \left(p_{\mathrm{H2O,w}} - p_{\mathrm{H2O,d}}\right) \tag{23}$$

where J is the molar flux across the membrane and $p_{\mathrm{H2O,d}}$ and $p_{\mathrm{H2O,w}}$ are the partial pressures in two adjacent control volumes on the humidifier's dry and wet side [42]. The permeability σ_{mem} is a material parameter that includes the combined effects of the sorption coefficient and diffusion coefficient. It is considered with a lookup table $\sigma_{\mathrm{mem}} = f(RH_{\mathrm{w}}, T)$ based on manufacturer data for the investigated Fumasep F-1020-RF membrane [39].

A mass balance for the $2n$ control volumes results in a system of ordinary differential equations

$$\frac{d\mathbf{X}_{\mathrm{H2O,d}}}{dt} = \frac{\dot{\mathbf{n}}_{\mathrm{H2O,in,d}} + \dot{\mathbf{n}}_{\mathrm{H2O,mem,d}} - \mathbf{X}_{\mathrm{H2O,d}} \dot{\mathbf{n}}_{\mathrm{tot,out,d}}}{\mathbf{n}_{\mathrm{tot,d}}} \tag{24}$$

$$\frac{d\mathbf{X}_{\mathrm{H2O,w}}}{dt} = \frac{\dot{\mathbf{n}}_{\mathrm{H2O,in,w}} + \dot{\mathbf{n}}_{\mathrm{H2O,mem,w}} - \mathbf{X}_{\mathrm{H2O,w}} \dot{\mathbf{n}}_{\mathrm{tot,out,w}}}{\mathbf{n}_{\mathrm{tot,w}}} \tag{25}$$

where $\mathbf{X}_{\mathrm{H2O,d}} \in \mathbb{R}^n$ and $\mathbf{X}_{\mathrm{H2O,w}} \in \mathbb{R}^n$ are molar fractions of water vapor in

Table 2
Terms of the mass balance equations of the humidifier model.

Variable	Equation
Molar flow into wet side control volume (mol/s)	$\dot{\mathbf{n}}_{\mathrm{H2O,in,w}_i} = \begin{cases} \dot{n}_{\mathrm{hm,w,in}} X_{\mathrm{H2O,w,in}} & \text{for } i = 1 \\ \dot{\mathbf{n}}_{\mathrm{H2O,out,w}_{i-1}} & \text{for } i = 2, \cdots, n \end{cases}$
Molar flow of water out of wet side control volume (mol/s)	$\dot{\mathbf{n}}_{\mathrm{H2O,out,w}_i} = \dot{\mathbf{n}}_{\mathrm{H2O,in,w}_i} + \dot{\mathbf{n}}_{\mathrm{H2O,mem,w}_i}$ for $i = 1, \cdots, n$
Molar flow across wet side membrane surface (mol/s) [42]	$\dot{\mathbf{n}}_{\mathrm{H2O,mem,w}_i} = \frac{\left(\frac{A_{\mathrm{mem}}}{n}\right)\sigma_{\mathrm{mem}i}}{\delta_{\mathrm{hm,mem}}} \left(\mathbf{p}_{\mathrm{hm,d}_i} \mathbf{X}_{\mathrm{H2O,d}_i} - \mathbf{p}_{\mathrm{hm,w}_i} \mathbf{X}_{\mathrm{H2O,w}_i}\right)$ for $i = 1, \cdots, n$
Permeability of membrane (mol s kg^{-1})	$\sigma_{\mathrm{mem}i} = f\left(T_{\mathrm{hm}}, \mathbf{RH}_{\mathrm{hm,w}_i}\right)$ for $i = 1, \cdots, n$
Relative humidity of wet side control volume (-)	$\mathbf{RH}_{\mathrm{hm,w}_i} = \frac{\mathbf{p}_{\mathrm{hm,w}_i} \mathbf{X}_{\mathrm{H2O,w}_i}}{p_{\mathrm{sat}}}$ for $i = 1, \cdots, n$
Total molar flow out of wet side control volume (mol/s)	$\dot{\mathbf{n}}_{\mathrm{tot,out,w}} = \begin{cases} \dot{n}_{\mathrm{hm,w,in}} + \dot{\mathbf{n}}_{\mathrm{H2O,mem,w}} & \text{for } i = 1 \\ \dot{\mathbf{n}}_{\mathrm{tot,in,w}_{i-1}} + \dot{\mathbf{n}}_{\mathrm{H2O,mem,w}} & \text{for } i = 2, \cdots, n \end{cases}$
Amount of substance in wet side control volume (mol)	$\mathbf{n}_{\mathrm{tot,w}_i} = \frac{\mathbf{p}_{\mathrm{hm,w}_i} \left(\frac{V_{\mathrm{hm,w}}}{n}\right)}{R T_{\mathrm{hm}}}$ for $i = 1, \cdots, n$
Pressure in wet side control volume (Pa)	$\mathbf{p}_{\mathrm{hm,w}_i} = p_{\mathrm{hm,w,in}} - i\left(\frac{\Delta p_{\mathrm{hm,w}}}{n}\right) + \frac{1}{2}\left(\frac{\Delta p_{\mathrm{hm,w}}}{n}\right)$ for $i = 1, \cdots, n$
Molar flow of water into dry side control volume (mol/s)	$\dot{\mathbf{n}}_{\mathrm{H2O,in,d}_i} = \begin{cases} \dot{\mathbf{n}}_{\mathrm{H2O,out,d}_{i+1}} & \text{for } i = 1, \cdots, n-1 \\ \dot{n}_{\mathrm{hm,d,in}} X_{\mathrm{H2O,d,in}} & \text{for } i = n \end{cases}$
Molar flow of water out of dry side control volume (mol/s)	$\dot{\mathbf{n}}_{\mathrm{H2O,out,d}_i} = \dot{\mathbf{n}}_{\mathrm{H2O,in,d}_i} + \dot{\mathbf{n}}_{\mathrm{H2O,mem,d}_i}$ for $i = 1, \cdots, n$
Molar flow across dry side membrane surface (mol/s)	$\dot{\mathbf{n}}_{\mathrm{H2O,mem,d}} = -\dot{\mathbf{n}}_{\mathrm{H2O,mem,w}}$
Total molar flow out of dry side control volume (mol/s)	$\dot{\mathbf{n}}_{\mathrm{tot,out,d}_i} = \begin{cases} \dot{\mathbf{n}}_{\mathrm{tot,out,d}_{i+1}} + \dot{\mathbf{n}}_{\mathrm{H2O,mem,d}_i} & \text{for } i = 1, \cdots, n-1 \\ \dot{n}_{\mathrm{hm,d,in}} + \dot{\mathbf{n}}_{\mathrm{H2O,mem,d}_i} & \text{for } i = n \end{cases}$
Amount of substance in dry side control volume (mol)	$\mathbf{n}_{\mathrm{tot,d}_i} = \frac{\mathbf{p}_{\mathrm{hm,d}_i} \left(\frac{V_{\mathrm{hm,d}}}{n}\right)}{R T_{\mathrm{hm}}}$ for $i = 1, \cdots, n$
Pressure in dry side control volume (Pa)	$\mathbf{p}_{\mathrm{hm,d}_i} = p_{\mathrm{hm,d,in}} - i\left(\frac{\Delta p_{\mathrm{hm,d}}}{n}\right) + \frac{1}{2}\left(\frac{\Delta p_{\mathrm{hm,d}}}{n}\right)$ for $i = 1, \cdots, n$

the control volumes on the dry and wet side, $\dot{\mathbf{n}}$ denotes a molar flow to or from a control volume and $\mathbf{n}_{tot}$ denotes the total amount of substance (in mol) in a control volume. The variables $\dot{\mathbf{n}}$ and $\mathbf{n}$ are vectors of size $\mathbb{R}^n$ whose elements are given in Table 2. The system of equations is solved numerically for its steady state with MATLAB's solver *ode15s*.

The stack's cathode exhaust temperature is approximately equal to the stack temperature ($T_{hm,w,in} = T_{stack,cw,out} = 85$ °C). The dry side inlet temperature $T_{hm,d,in}$ is controlled to the same value with the air cooler and its bypass (see section 3.3.4). The model therefore assumes that the two fluid streams have the same temperature T_{hm} at each location in the humidifier.

3.2.2. Pressure drop characteristic

The pressures in the control volumes $\mathbf{p}_{hm,w}$ and $\mathbf{p}_{hm,d}$ are determined by splitting the overall pressure drop of the respective side equally to each control volume. The overall pressure drop on the humidifier's dry and wet side are approximated with empirical correlations

$$\Delta p_{hm,d} = k_{hmd1}\left(\frac{\dot{m}_{hm,d,in}}{N_{hm,tube}}\right)^2 + k_{hmd2}\left(\frac{\dot{m}_{hm,d,in}}{N_{hm,tube}}\right) \tag{26}$$

$$\Delta p_{hm,w} = k_{hmw1}\left(\frac{\dot{m}_{hm,d,in}}{N_{hm,tube}}\right)^2 + k_{hmw2}\left(\frac{\dot{m}_{hm,d,in}}{N_{hm,tube}}\right) \tag{27}$$

where the coefficients k are fitted to literature data (see Table 3). Because the correlations depend on the mass flow per tube, they can also approximate pressure drops of a humidifier with a different number of parallel tubes of the same length.

3.2.3. Model parameterization

The humidifier model that is used for the overall system sizing is parameterized with manufacturer data for a Fumatech Ecomate H50 humidifier [39,43]. To validate the modelling approach with experimental data from Tallgren et al. [44], the model is also parameterized with data for a H20 humidifier [45]. The H20 humidifier is a smaller but otherwise similar version of the H50 type. The model's parameters are given in Table 3. The ratio $r_{hm,V}$ from Eq. (22) is fitted to manufacturer data by minimizing the difference between the predicted and actual ADT_{hm}. The tube diameter is assumed based on the H10N humidifier that is used in the stack test bench (section 3.1.1).

Table 3
Parameters for two membrane humidifiers from the Fumatech Ecomate series [39].

Parameter	Symbol	Fumatech H20	Fumatech H50	Reference/ Background
Rated dry air flow (kg/s)	$\dot{m}_{hm,d,in}$	0.026	0.052	[39]
Rated approach dew point temperature (°C)	ADT_{hm}	13	11	[39]
Mass (kg)	m_{hm}	5	6	[39]
Core volume (m^3)	$V_{hm,core}$	7	11	[39]
Tube wall thickness (µm)	$\delta_{hm,tube}$	20	20	[46]
Tube length (mm)	$l_{hm,tube}$	230	280	[43,45]
Ratio of dry and wet volume (-)	$r_{hm,V}$	0.132	0.256	Fitted (H20: [39], H50: [39])
Number of tubes	$N_{hm,tube}$	5914	6730	Based on fitted $r_{hm,V}$
Dry side pressure drop coefficient (-)	k_{hmd1}	$7.253 \cdot 10^{13}$	$-2.037 \cdot 10^{13}$	Fitted (H20: [44], H50: [39])
Dry side pressure drop coefficient (-)	k_{hmd2}	$5.130 \cdot 10^{8}$	$1.518 \cdot 10^{9}$	Fitted (H20: [44], H50: [39])
Wet side pressure drop coefficient (-)	k_{hmw1}	$3.074 \cdot 10^{14}$	$-1.586 \cdot 10^{9}$	Fitted (H20: [44], H50: [39])
Wet side pressure drop coefficient (-)	k_{hmw2}	$-1.605 \cdot 10^{8}$	$3.205 \cdot 10^{9}$	Fitted (H20: [44], H50: [39])

3.2.4. Integration into the overall system model

The humidifier is sized to achieve a given relative humidity $RH_{hm,d,out}$ at the stack's cathode inlet. This is done by solving Eqs. (18) to (27) iteratively for varying number of tubes until the dry side outlet relative humidity matches the desired value. The core volume $V_{hm,core}$ is then determined with Eqs. (20) to (22). The header volume $V_{hm,head}$ is assumed to increase the total volume V_{hm} by an additional 10 %. The mass of the humidifier is approximated with an empirical correlation.

$$m_{hm} = 415.3846 V_{hm,core} + 1.6154 \tag{28}$$

Eq. (28) is derived from the mass (in kg) and volume (in m^3) of different humidifier sizes in the Fumatech Ecomate series with rated air mass flows between 0.005 and 0.104 kg/s [39].

When simulating a previously sized humidifier, the model calculates $RH_{hm,d,out}$ for different operating points and a fixed number of tubes. The humidity at the stack's inlet is controlled by partially bypassing the humidifier's dry side in some operating points (see Fig. 1 (c)). The bypass ratio is defined as

$$b_{hm} = 1 - \frac{\dot{n}_{hm,d,in}}{\dot{n}_{cp}/N_{stack}} \tag{29}$$

where $\dot{n}_{cp}/N_{stack}$ is the molar flow of compressed air per stack. When sizing the humidifier for the point with the highest humidification requirement, $b_{hm} = 0$. When simulating a previously sized humidifier for an operating point that requires less humidification, $0 \leq b_{hm} \leq 1$. To maintain a low computational cost, b_{hm} is not calculated explicitly during the simulations. Instead, Eqs. (18) to (27) are solved once for $b_{hm} = 0$ to verify that the maximum achievable relative humidity is larger than the required value. The dry side pressure drop $\Delta p_{hm,d} = f(\dot{n}_{hm,d,in})$ for $b_{hm} = 0$ is used as a worst-case approximation of the actual pressure drop (bypassing the humidifier would result in a somewhat reduced air flow and hence a somewhat lower pressure drop).

3.3. Heat exchanger

The model is used to size the system's heat exchangers and to simulate their behavior at various operating points. It considers louvered-fin heat exchangers, which are typically chosen for fuel cell cooling in aircraft [10,16] and automotive applications [12,27,47]. In the air-to-liquid case (fuel cell cooler and compressor cooler), the louvered-fin surfaces are combined with flat tubes for the liquid coolant. In the air-to-air case (air cooler), both the hot and the cold side are equipped with louvered-fin surfaces. The following subsections describe the governing equations for a given set of geometric parameters (e.g. fin length, fin pitch), which are defined in detail in Appendix B.

3.3.1. Heat transfer

The transferred heat flow is given by

$$\dot{Q}_{hx} = \dot{m}_{hx,h} c_{p,h} (T_{hx,h,in} - T_{hx,h,out}) \tag{30}$$

$$\dot{Q}_{hx} = \dot{m}_{hx,c} c_{p,c} (T_{hx,c,out} - T_{hx,c,in}) \tag{31}$$

where $\dot{m}_{hx}$ is the mass flow, T_{hx} the temperature and c_p the specific heat capacity. The subscripts "h" and "c" denote the hot and cold side, "in" and "out" denote the inlet and outlet of the respective side. Heat losses to

the surroundings are neglected [47,48]. The effectiveness is defined as [47]

$$\varepsilon_{\mathrm{hx,req}} = \frac{C_{\mathrm{h}}(T_{\mathrm{hx,h,in}} - T_{\mathrm{hx,h,out}})}{C_{\min}(T_{\mathrm{hx,h,in}} - T_{\mathrm{hx,c,in}})} \tag{32}$$

$$C_{\mathrm{h}} = \dot{m}_{\mathrm{hx,h}} c_{\mathrm{p,h}} \tag{33}$$

$$C_{\mathrm{c}} = \dot{m}_{\mathrm{hx,c}} c_{\mathrm{p,c}} \tag{34}$$

where C_{h}, C_{c} and $C_{\min} = \min(C_{\mathrm{h}}, C_{\mathrm{c}})$ are the stream capacity rates. For a crossflow heat exchanger with unmixed streams, it is related to the number of transfer units Ntu via Eq. (35) [47].

$$\varepsilon_{\mathrm{hx}} = 1 - \exp\left(\left(\exp\left(-Ntu^{0.78} C^{*}\right) - 1\right) Ntu^{0.22} / C^{*}\right) \tag{35}$$

$$C^{*} = \frac{C_{\min}}{C_{\max}}$$

$$Ntu = \frac{u A_{\mathrm{s,eff}}}{C_{\min}} \tag{36}$$

The heat transfer conductance $uA_{\mathrm{s,eff}}$ across a simplified one-dimensional geometry is given by [47]

$$\frac{1}{uA_{\mathrm{s,eff}}} = \frac{1}{\eta_{\mathrm{o,h}} \alpha_{\mathrm{h}} A_{\mathrm{s,h}}} + \frac{T_{\mathrm{t}}}{\lambda_{\mathrm{wall}} A_{\mathrm{s,tube}}} + \frac{1}{\eta_{\mathrm{o,c}} \alpha_{\mathrm{c}} A_{\mathrm{s,c}}} \tag{37}$$

where the first and third term are the thermal resistances of the hot and cold side boundary layers and the second term is the wall resistance. The parameter $\lambda_{\mathrm{wall}}(T_{\mathrm{wall}})$ is the thermal conductivity of aluminum [47], T_{t} the tube wall thickness and $A_{\mathrm{s,tube}}$ the tube surface area (see Appendix B). The wall temperature is approximated with Eq. (38) to avoid the computational cost of an iterative solution.

$$T_{\mathrm{wall}} = \left(\frac{T_{\mathrm{hx,c,in}} + T_{\mathrm{hx,c,out}}}{2} + \frac{T_{\mathrm{hx,h,in}} + T_{\mathrm{hx,h,out}}}{2}\right)/2 \tag{38}$$

The heat transfer across the fin geometry is modelled based on the surface area A_{s} (see Appendix B) and the surface effectiveness η_{o} of the respective side. The mean heat transfer coefficient α is given by [47,48]

$$\alpha = \frac{Nu \lambda_{\mathrm{fl}}}{l_{\mathrm{hx}}} \tag{39}$$

where Nu is the dimensionless Nusselt number, $\lambda_{\mathrm{fl}}(T_{\mathrm{wall}})$ is the thermal conductivity of the respective fluid and l_{hx} the characteristic length of the respective side (see Table 4). Empirical correlations express the relation $Nu(Re)$ as a function of the geometric parameters (see Table 4). The Reynolds number Re is calculated based on the velocity c as well as the density $\rho(p,T)$ and dynamic viscosity $\mu(T)$ of the respective fluid.

$$Re = \frac{\rho c l_{\mathrm{hx}}}{\mu} \tag{40}$$

$$c = \frac{\dot{m}}{\rho A_{\mathrm{cr}}} \tag{41}$$

A_{cr} is the cross-section area of each heat exchanger side (see Appendix B).

The correlations for the louvered-fin surface were originally developed for an air-to-liquid heat exchanger and depend on the tube geometry (tube pitch T_{p} and tube major diameter D_{m}). It is assumed that the hot air side in the crossflow air-to-air heat exchanger has nearly the same flow blockage effect on the cold air side as a tube (and vice versa). The model therefore uses the same correlations for the air-to-air case. The corresponding equivalent parameters $T_{\mathrm{p,eq}}$ and $D_{\mathrm{m,eq}}$ for the air-to-air case are defined in Appendix B.

The surface effectiveness η_0 is given by [47]

$$\eta_0 = 1 - (1 - \eta_{\mathrm{f}}) \frac{A_{\mathrm{fin}}}{A_{\mathrm{s}}} \tag{42}$$

$$\eta_{\mathrm{f}} = \tanh\left(\frac{F_{\mathrm{l}}}{2}\sqrt{\frac{2\alpha}{\lambda_{\mathrm{wall}} F_{\mathrm{t}}}}\right)\left(\frac{F_{\mathrm{l}}}{2}\sqrt{\frac{2\alpha}{\lambda_{\mathrm{wall}} F_{\mathrm{t}}}}\right)^{-1} \tag{43}$$

where F_{l} is the fin length, F_{t} is the fin thickness and A_{fin} is the fin surface area (see Appendix B). For the liquid side, $\eta_0 = 1$ because the tubes contain no secondary surfaces.

3.3.2. Pressure drop

The pressure drop of the hot and cold side of the heat exchanger core is [47,48]

$$\Delta p_{\mathrm{hx}} = \frac{1}{2} \rho c^2 \frac{4 L_{\mathrm{hx}}}{d_{\mathrm{h}}} f_{\mathrm{fric}} \tag{44}$$

where L_{hx} is the flow length of the respective side (see Table 4), d_{h} is the hydraulic diameter (see Appendix B) and f_{fric} is the dimensionless Fanning friction factor. The friction factor $f_{\mathrm{fric}}(Re)$ is determined with the

Table 4
Correlations for Nusselt number Nu and Fanning friction factor f_{fric}. The geometric variables are defined in Appendix B.

Surface type	Characteristic length	Flow length	Correlation
Louvered fin	$l_{\mathrm{hx}} = L_{\mathrm{p}}$	$L_{\mathrm{hx}} = F_{\mathrm{d}}$	*For 100 < Re < 3000* Correlations are given in refs. [49,50]. $Nu = jRePr^{1/3}$ $j = f(Re, \Theta, L_{\mathrm{p}}, F_{\mathrm{p}}, F_{\mathrm{l}}, L_{\mathrm{l}}, T_{\mathrm{p}}, F_{\mathrm{d}}, F_{\mathrm{t}})$ $f_{\mathrm{fric}} = f(Re, \Theta, L_{\mathrm{p}}, F_{\mathrm{p}}, F_{\mathrm{l}}, L_{\mathrm{l}}, T_{\mathrm{p}}, F_{\mathrm{t}}, D_{\mathrm{h}})$
Flat tube	$l_{\mathrm{hx}} = d_h$	$L_{\mathrm{hx}} = T_{\mathrm{l}}$	*For laminar flow (Re ≤ 2300)* [48]: $Nu = \frac{3.657}{\tanh(2.264X^{1/3} + 1.7X^{2/3})} + \frac{0.0499}{X}\tanh(X)X = T_{\mathrm{l}}/(d_{\mathrm{h}}RePr)$ $f_{\mathrm{fric}} = 16/Re$ *For transitional flow (2300 < Re < 4000):* Sizing: Transitional regime is not considered because of uncertainty in the correlations [47] Simulation: Transitional regime is approximated with linear interpolation between the laminar ($Re = 2300$) and turbulent ($Re = 4000$) values for Nu and f_{fric} *For turbulent flow (4000 ≤ Re ≤ 10^6)* [48]: $Nu = \frac{(\frac{\zeta}{8})(Re - 1000)Pr}{1 + 12.7\sqrt{\frac{\zeta}{8}}(Pr^{2/3} - 1)}\left(1 + \left(\frac{d_{\mathrm{h}}}{T_{\mathrm{l}}}\right)^{2/3}\right)\left(\frac{Pr}{Pr_0}\right)^{0.11}$ $\zeta = (0.78\ln(Re) - 1.5)^{-2}$ is the Moody friction factor $Pr_0 = Pr(T_{\mathrm{wall}})$ is the Prandtl number (valid for $0.1 \le Pr \le 1000$ and $T_{\mathrm{l}}/d_{\mathrm{h}} > 1$) $f_{\mathrm{fric}} = \zeta/4$

correlations in Table 4. The pressure drop in the headers is neglected.

3.3.3. Optimal sizing of heat exchangers

Eqs. (30) to (44) define the dependence of the effectiveness ε_{hx} on the heat exchanger's geometric parameters. The resulting mass m_{hx} for a set of geometric parameters is calculated according to Appendix B. When sizing the heat exchangers, the goal is to find the best combination of geometric parameters that can meet the sizing requirements. This sizing task is viewed as a constrained nonlinear optimization problem

$$\underset{\mathbf{x}_{hx}}{\text{minimize}}\ m_{hx}(\mathbf{x}_{hx})$$

subject to

$$\varepsilon_{hx,j}(\mathbf{x}_{hx}) \geq \varepsilon_{hx,req,j} \quad \text{for } j = 1, \cdots, N_s$$

$$\Delta\mathbf{p}_{hx,c,j}(\mathbf{x}_{hx}) \leq \Delta\mathbf{p}_{hx,c,max,j} \quad \text{for } j = 1, \cdots, N_s$$

$$\Delta\mathbf{p}_{hx,h,j}(\mathbf{x}_{hx}) \leq \Delta p_{hx,h,max} \quad \text{for } j = 1, \cdots, N_s$$

$$\mathbf{lb}_{hx,i} \leq \mathbf{x}_{hx,i} \leq \mathbf{ub}_{hx,i} \quad \text{for } i = 1, \cdots, 6$$

$$\mathbf{A}_{hx,front}(\mathbf{x}_{hx}) \leq A_{hx,front,max}$$

where the vector $\mathbf{x}_{hx} \in \mathbb{R}^6$ contains the optimized geometric parameters from Appendix B, Table B.1. The effectiveness and the pressure drop are constrained by the requirements in each of the $N_s = 7$ investigated flight phases (see section 4). In addition, the frontal area $\mathbf{A}_{hx,front}$ is constrained to a maximum value (see section 4). The optimization problem is solved by evaluating the underlying equations for a large, discrete set of input combinations and using the best of these combinations as the presumed global minimum (brute-force approach). The chosen upper and lower bound $\mathbf{ub}_{hx,i}$ and $\mathbf{lb}_{hx,i}$ for each element of $\mathbf{x}_{hx}$ are given in Appendix B, Table B.1.

3.3.4. Heat exchanger simulation

The outlet temperature of the hot side fluid is controlled by partially bypassing the hot side of the heat exchangers (see Fig. 1 (c)). The bypass ratio b_{hx} is defined as

$$b_{hx} = \frac{\dot{m}_{hx,pb}}{\dot{m}_{hx,pb} + \dot{m}_{hx,h}} \tag{45}$$

where $\dot{m}_{hx,pb}$ is the bypassed mass flow. The temperature after mixing $\dot{m}_{hx,pb}$ with the flow through the heat exchanger $\dot{m}_{hx,h}$ is given by

$$T_{h,mix} = \frac{\dot{m}_{hx,pb}T_{bp} + \dot{m}_{hx,h}T_{hx,h,out}}{\dot{m}_{hx,pb} + \dot{m}_{hx,h}} \tag{46}$$

where $T_{bp} = T_{hx,h,in}$ is the temperature of the bypassed flow. When sizing the heat exchanger, $b_{hx} = 0$.

When the behavior of a previously sized heat exchanger is simulated for different operating points, $T_{hx,h,out}$ becomes an unknown parameter. In that case, Eqs. (30) to (44) form a system of equations that is numerically solved for $T_{hx,h,out}$. Next, Eqs. (45) and (46) are solved for the required ratio b_{hx} to achieve the desired $T_{h,mix}$.

3.4. Compressor

The compressor model determines the power consumption of the compressor at different air mass flows, ambient pressures and stack operating pressures. The enthalpy change in a single stage is [51]

$$\Delta h_{cp} = \frac{\bar{c}_{p,air}T_{cp,in}}{\eta_{cp,s}}\left(\left(\Pi_{cp}\right)^{\frac{R_{sp,air}}{\bar{c}_{p,air}}} - 1\right) \tag{47}$$

where $\eta_{cp,s}$ is the isentropic compressor efficiency, $R_{sp,air}$ the specific gas constant and $\Pi_{cp} = p_{cp,out}/p_{cp,in}$ the pressure ratio. The difference of fluid velocity between the compressor inlet and outlet is neglected [51]. Because of the large difference between the inlet and outlet temperatures $T_{cp,in}$ and $T_{cp,out}$, the mean specific heat capacity is used. It is evaluated with

$$\bar{c}_{p,air} = \frac{1}{T_{cp,out} - T_{cp,in}}\int_{T_{cp,in}}^{T_{cp,out}} c_{p,air}(T)dT \tag{48}$$

where $c_{p,air}(T)$ is evaluated from a lookup table with 1 °C increments from ref. [29]. The outlet temperature is given by Eq. (49).

$$T_{cp,out} = \frac{\bar{c}_{p,air}T_{cp,in} + \Delta h_{cp}}{\bar{c}_{p,air}} \tag{49}$$

Eqs. (47) to (49) are solved numerically for $T_{cp,out}$ with MATLAB's solver *fminsearch*. The compressor's power consumption is calculated with

$$P_{cp} = \frac{\Delta h_{cp}\dot{m}_{cp}}{\eta_{cp,m}\eta_{cp,el}\eta_{cp,pc}} \tag{50}$$

where $\eta_{cp,m}$, $\eta_{cp,el}$ and $\eta_{cp,pc}$ are the mechanical efficiency, electric motor efficiency and power converter efficiency (see Table 5). The non-isentropic compression increases the temperature of the compressed fluid. The losses in the drive-train components result in an additional waste heat flow that is removed with a liquid cooling loop.

$$\dot{Q}_{cp,liq} = \Delta h_{cp}\dot{m}_{cp}\left(\frac{1}{\eta_{cp,m}\eta_{cp,el}} - 1\right) \tag{51}$$

The coolant is a 50 % (volume/volume) mixture of water and ethylene glycol [52]. For the investigated compressor designs [25,53], the coolant pump is integrated into the compressor housing and is therefore accounted for with the mass and mechanical efficiency of the compressor. The cooling of the power converters is not considered by the model (see system boundary definition in section 2).

Table 5
Compressor model parameters. Mechanical components based on Rotrex C38-91 [25], electric motor and power converter based on Rotrex EK 40 [52] (linearly scaled to the same baseline mass flow of 0.63 kg/s).

Parameter	Symbol	Value
Mechanical efficiency [25]	$\eta_{cp,m}$	0.97
Electric motor efficiency [54]	$\eta_{cp,el}$	0.94
Power converter efficiency (stack to DC bus) [54]	$\eta_{DC/DC}$	0.97
Power converter efficiency (DC bus to electric motor) [54]	$\eta_{DC/AC}$	0.97
Overall power converter efficiency	$\eta_{cp,pc}$	0.97·0.97
Maximum mass flow of baseline design [25]	$\dot{m}_{cp,max,base}$	0.63 kg/s
Mass of mechanical compressor components for baseline design [25]	$m_{cp,m,base}$	6.0 kg
Mass of electric motor for baseline design [52]	$m_{cp,el,base}$	80.1 kg
Mass of power converter for baseline design [52]	$m_{cp,pc,base}$	17.9 kg
Volume of mechanical compressor components for baseline design [25]	$V_{cp,m,base}$	0.0105 m^3
Volume of electric motor for baseline design [52]	$V_{cp,el,base}$	0.0610 m^3
Volume of power converter for baseline design [52]	$V_{cp,pc,base}$	0.0239 m^3
Cross-section inlet area of baseline design [25]	$A_{cp,in,base}$	0.0038 m^2
Compressor coolant temperature [52]	$T_{cp,cw,in}$	50 °C

3.4.1. Performance characteristic

The variation of rotational speed and efficiency in different operating points is considered with scaled empirical compressor maps. The maps are included with the well-known Jensen-Kristensen approach [55,56], which describes the compressor's rotational speed and isentropic efficiency with semi-empirical analytic functions.

$$n_{cp,red} = f(\dot{m}_{cp,red}, \Pi_{cp}, k_{n,ij}) \tag{52}$$

$$\eta_{cp,s} = f(\dot{m}_{cp,red}, n_{cp,red}, k_{e,ij}) \tag{53}$$

The underlying expressions and parameters for Eqs. (52) and (53) are described in Appendix C. The coefficients $k_{n,ij}$ and $k_{e,ij}$ are fitted with publicly available manufacturer data for a Rotrex C38-91 radial turbo-compressor [25]. The datapoints that are used to fit these coefficients are described in Appendix C.

The actual mass flow $\dot{m}_{cp}$ and rotational speed n_{cp} are scaled to reduced quantities $\dot{m}_{cp,red}$ and $n_{cp,red}$ based on the well-known Mach number similarity concept [24,56,57].

$$\dot{m}_{cp,red} = \dot{m}_{cp}\frac{p_{ref}}{p_{cp,in}}\sqrt{\frac{T_{cp,in}}{T_{ref}}} \tag{54}$$

$$n_{cp,red} = n_{cp}\sqrt{\frac{T_{ref}}{T_{cp,in}}} \tag{55}$$

The reference conditions are $T_{ref} = 15\ °C$ and $p_{ref} = 1.013$ bar in this case [25].

3.4.2. Effect of the altitude

It is well known that a compressor's operating map changes for different inlet pressures and temperatures [24,57]. This results in different rotational speeds and efficiencies at different flight altitudes. The Mach number similarity concept is used to consider this effect in a computationally efficient way: First, the coefficients of Eqs. (52) and (53) are fitted to the reduced compressor map in terms of $\dot{m}_{cp,red}$ and $n_{cp,red}$. Next, Eqs. (54) and (55) are used to modify the compressor map based on the inlet temperature and pressure of the respective flight phase [24,57]. According to Li et al. [15], such correction methods can lead to inaccurate results above altitudes of 2000 to 3000 m. However, in the case of a single-stage radial compressor it was shown that the Mach number similarity concept provides reasonable accuracy up to at least 5500 m [57]. Therefore, Eqs. (54) and (55) are assumed to be sufficiently accurate for the purpose of this study.

3.4.3. Effect of varying compressor sizes

The effect of varying compressor sizes is modelled with scaled empirical compressor maps. Refs. [25,53] provide rotational speed maps and efficiency maps of multiple compressors from the same manufacturer with varying maximum rated mass flows (0.48 kg/s to 0.84 kg/s) and pressure ratios (2.82 to 3.38). All these maps result in approximately the same shape and limits when normalizing them based on their respective point of maximum efficiency at the same rotational speed (60 krpm). By normalizing the rotational speed map and efficiency map for one of these compressors, one can therefore predict the maps of other geometrically similar compressors with reasonable accuracy. The model uses Eqs. (56) and (57) to obtain the normalized rotational speed and efficiency maps based on a Rotrex C38-91 compressor [25]. This approach is validated in section 5.1.4.

$$\dot{m}_{cp,norm} = \frac{\dot{m}_{cp,red}}{\left(\dot{m}_{cp,red}\right)_{\eta_{cp,s,max}}} \tag{56}$$

$$\Pi_{cp,norm} = \frac{\Pi_{cp}}{\left(\Pi_{cp}\right)_{\eta_{cp,s,max}}} \tag{57}$$

The mass, volume and inlet area $A_{cp,in}$ of different compressor sizes are approximated by linearly scaling the properties a baseline design (see Table 5) with the compressor's maximum mass flow.

$$m_{cp} = \frac{\left(m_{cp,m,base} + m_{cp,el,base} + m_{cp,pc,base}\right)\dot{m}_{cp,red,max}}{\dot{m}_{cp,red,max,base}} \tag{58}$$

$$V_{cp} = \frac{\left(V_{cp,m,base} + V_{cp,el,base} + V_{cp,pc,base}\right)\dot{m}_{cp,red,max}}{\dot{m}_{cp,red,max,base}} \tag{59}$$

$$A_{cp,in} = A_{cp,in,base}\frac{\dot{m}_{cp,red,max}}{\dot{m}_{cp,red,max,base}} \tag{60}$$

The effect of the maximum pressure ratio on m_{cp}, V_{cp} and $A_{cp,in}$ is small in the investigated range [25,53] and is therefore neglected.

3.4.4. Feasible operating range

For a given pressure ratio, the compressor's feasible mass flow is limited by its surge and choke line as well as its minimum and maximum rotational speed [24]. The model considers these four limiting conditions with lookup tables that contain the respective datapoints of the normalized Rotrex C38-91 compressor map. Eqs. (56) and (57) are used to scale the lookup table values $\dot{m}_{cp,red}$ and $\Pi_{cp,red}$ to the respective compressor size. The effect of different inlet pressures and temperatures is considered with Eqs. (54) and (55). The surge control limit is chosen as the surge line with an additional 10 % mass flow margin [58]. If the required mass flow is below the compressor's surge control limit, the mass flow is increased and the excess compressed air is vented to the surroundings (see Fig. 1 (c)) [7]. This approach results in a somewhat reduced system efficiency in some operating points, but avoids the complexity of having multiple compressor units to meet the mass flow requirements.

3.5. Additional component models

The system's diffusers and nozzles (see Fig. 1 (c)) are modelled based on the equations in Table 6. The inlet and exit areas of each diffuser $A_{dr,in}$ and $A_{dr,out}$ are design parameters that are set at the system level (see section 4). The controllable outlet area $A_{nz,out}$ is chosen to expand the flow to the ambient pressure ($p_{nz,out} = p_{amb}$) of the respective flight phase. In this manner, the maximum feasible outlet velocity is achieved, which in turn minimizes the system's drag.

The coolant pump and anode recirculation blower have a small impact on the overall system performance (see section 5.2). Hence, they are considered with simpler models based on constant component efficiencies as described in Appendix D.

The pressure drop in the stack, humidifier and heat exchangers is considered with Eqs. (8), (26), (27), (44) as well as Eqs. (A.7) and (D.8)

Table 6
Governing equations for the diffuser and nozzle model.

Variable	Equation
Air-inlet	
Mass flow (m/s)	$\dot{m}_{dr} = c_{dr,i}\rho A_{dr,i}$ for i ={in, out}
Diffuser isentropic efficiency definition (-) [60]	$\eta_{dr} = \frac{T_{dr,out,rev} - T_{dr,in}}{T_{dr,out} - T_{dr,in}}$
Assumed isentropic diffuser efficiency (-) [60]	$\eta_{dr} = 0.97$
Outlet temperature if process was isentropic (K)	$T_{dr,out,rev} = T_{dr,in}\left(\frac{p_{dr,out}}{p_{dr,in}}\right)^{R_{sp}/c_p}$
Actual outlet temperature (K) [60]	$T_{dr,out} = \frac{1}{2c_p}\left(c_{dr,in}{}^2 - c_{dr,out}{}^2\right) + T_{dr,in}$
Nozzle	
Fluid velocity (m/s)	$c_{nz,i} = \frac{\dot{m}_{dr}}{\rho A_{nz,i}}$ for i ={in, out}
Nozzle isentropic efficiency definition (-) [60]	$\eta_{nz} = \frac{T_{nz,in} - T_{nz,out}}{T_{nz,in} - T_{nz,out,rev}}$
Assumed isentropic nozzle efficiency (-) [60]	$\eta_{nz} = 0.95$
Outlet temperature if process was isentropic (K)	$T_{nz,out,rev} = T_{nz,in}\left(\frac{p_{nz,out}}{p_{nz,in}}\right)^{R_{sp}/c_p}$
Outlet velocity (m/s) [60]	$c_{nz,out} = \sqrt{2c_p\left(T_{nz,in} - T_{nz,out}\right) + c_{nz,in}{}^2}$

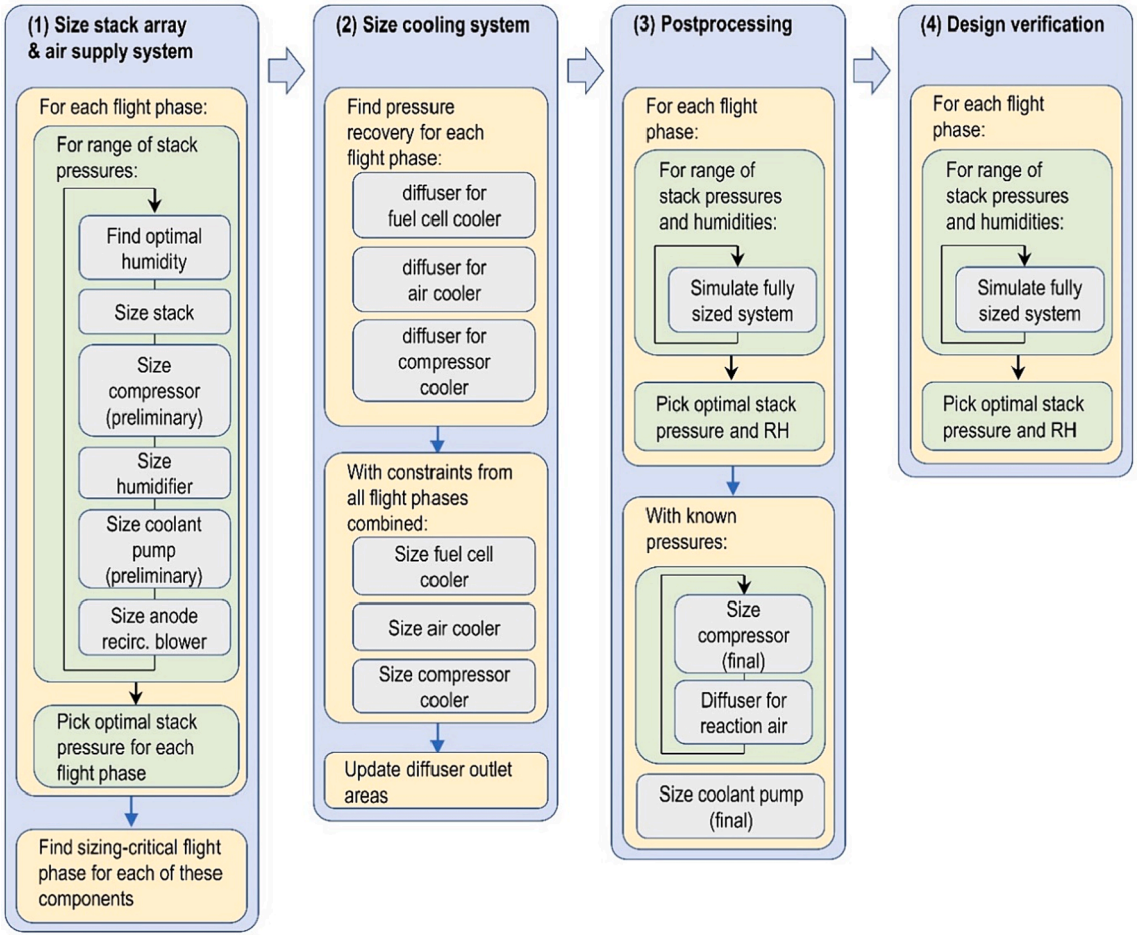

Fig. 3. The four stages of the overall system sizing process.

in the Appendix. The pressure drop of the piping between the system components will be significantly smaller than the pressure drop of the narrow channels in the stack, humidifier and heat exchangers. Hence, the pressure drop of the piping has a small impact on the overall system performance and is neglected. The pressure drop of the water separator is also negligibly small ($\leq$0.05 bar according to ref. [59]).

4. System sizing

The previous sections described the sizing approach for each individual component. The overall system sizing aims at finding the smallest combination of these individual component sizes that can fulfill the requirements of the aircraft's design mission. The sizing is conducted in an iterative process with four stages, which are summarized in Fig. 3. This iterative process is controlled by a number of design parameters, which are listed in Table 7. These design parameters can be used to optimize the system for contradicting design targets (such as a low mass or high efficiency). The remainder of this section describes the four stages of the sizing process and explains how the design parameters affect the system design. The pareto-optimization of the four most relevant design parameters is discussed in section 5.3.

4.1. Stacks and air supply system (stage 1)

The required stack power for a given net system power depends on the power consumption of the auxiliary components (see Eq. (1)). This leads to several circular dependencies: The stack power and compressor power depend on each other, because different stack powers lead to different air mass flows. This increases the compressor power directly via Eq. (50) and indirectly via the pressure losses Δp along the air path. Increased pressure losses affect the compressor power, because they increase the required pressure ratio Π_{cp} to achieve the desired pressure at the stack's inlet $p_{stack,C,in}$.

$$\Pi_{cp} = \frac{p_{stack,C,in} + \Delta p_{hm,d} + \Delta p_{hx,ac,h}}{p_{dr,out,react}} \tag{61}$$

Similarly, the stack power and the power consumption of the coolant pump depend on each other because a larger stack power requires a larger coolant mass flow. A larger stack power also leads to a larger hydrogen mass flow, which increases the required anode recirculation power P_{ar}. These dependencies are resolved by iteratively adjusting the component sizes until the required net power $P_{sys,eff}$ of the respective flight phase is achieved. At this stage, the following approximations are made: The pressure increase in the diffuser for reactant air is initially neglected, so that $p_{dr,out,react} = p_{amb}$. The pressure drop in the heat exchangers is initially approximated with the chosen maximum values $\Delta p_{HX,ac,h,max}$ and $\Delta p_{HX,FC,h,max}$. The stack's current density is initially kept constant at the chosen design value i_{des} (see Table 7). These approximations are replaced with more accurate results in stages 2 and 3. The chosen current density i_{des} determines the required number of stacks and cells per stack for a given stack power output via Eqs. (9) to (12). Higher i_{des} result in a lower stack mass for a given power output, while lower i_{des} result in an improved stack efficiency. Hence, this parameter can be used to trade a lower system mass for an improved system efficiency.

The iterative sizing is repeated for different stack pressures $p_{stack,C,in}$ to find the pressure that results in the highest system efficiency $\eta_{sys,LHV}$. The sizing process evaluates pressures between 1 and 2 bar abs. with 0.1

Table 7
Design parameters that control the overall system sizing process.

Design parameter	Symbol	Value in section 5.2	Value/range in section 5.3
Optimized parameters			
Current density at the system's rated load (A/cm^2)	i_{des}	0.6	[0.4,0.5,0.6,0.7,0.8,0.9,1.0]
Constraint for max. relative humidity at the stack's cathode inlet (-)	RH_{des}	0.5	[0.5,0.6,0.7,0.8]
Inlet area of diffuser for main fuel cell cooler, normalized with waste heat (m^2/W)	$a_{FC,in}$	$4.32 \cdot 10^{-7}$	[$4.32 \cdot 10^{-7}$, $4.80 \cdot 10^{-7}$, $5.28 \cdot 10^{-7}$]
Outlet area of diffuser for main fuel cell cooler, normalized with waste heat (m^2/W)	$a_{FC,out}$	$4.60 \cdot 10^{-6}$	[$3.76 \cdot 10^{-6}$, $4.18 \cdot 10^{-6}$, $4.60 \cdot 10^{-6}$]
Constant parameters			
Hot side pressure drop of fuel cell cooler (Pa)	$\Delta p_{hx,FC,h,max}$	$5 \cdot 10^3$	$5 \cdot 10^3$
Hot side pressure drop of air cooler (Pa)	$\Delta p_{hx,ac,h,max}$	$5 \cdot 10^3$	$5 \cdot 10^3$
Hot side pressure drop of compressor cooler (Pa)	$\Delta p_{hx,cp,h,max}$	$5 \cdot 10^3$	$5 \cdot 10^3$
Normalized compressor mass flow at sizing point (-)	$\dot{m}_{cp,norm}$	1.64	1.64
Inlet area of diffuser for air cooler, normalized with waste heat (m^2/W)	$a_{ac,in}$	$3.24 \cdot 10^{-7}$	$3.24 \cdot 10^{-7}$
Outlet area of diffuser for air cooler, normalized with waste heat (m^2/W)	$a_{ac,out}$	$4.50 \cdot 10^{-6}$	$4.50 \cdot 10^{-6}$
Inlet area of diffuser for compressor cooler, normalized with waste heat (m^2/W)	$a_{cp,in}$	$5.45 \cdot 10^{-7}$	$5.45 \cdot 10^{-7}$
Outlet area of diffuser for compressor cooler, normalized with waste heat (m^2/W)	$a_{cp,out}$	$5.02 \cdot 10^{-5}$	$5.02 \cdot 10^{-5}$

bar increments. The relative humidity at the stack's inlet $RH_{stack,C,in}$ is chosen to maximize the cell voltage. Since $RH_{stack,C,in}$ determines the required humidifier size, it is constrained to a maximum value RH_{des} (see Table 7). This design parameter can also be used to trade mass for efficiency: Larger RH_{des} enable higher stack efficiencies due to improved humidification, but result in an increased humidifier mass. The stack's operating temperature $T_{stack,cw,out}$ is kept constant at the assumed maximum permanent operating temperature of 85 °C to achieve a low cooling system drag. The reasoning behind this design choice is as follows: A larger temperature difference between the fuel cell coolant and the ambient air enables a larger temperature increase of the cooling air inside the heat exchanger. This reduces the required cooling air mass flow (see Eq. (31)), which in turn reduces the drag (see Eq. (5)). The stack's cathode stoichiometric ratio is kept constant at $\lambda_{O_2} = 1.7$ to minimize the compressor's power consumption [17]. After conducting the above steps for each flight phase, the size of the stacks and auxiliary components is chosen based on the maximum required size in all flight phases combined. The compressor is sized so that its rated operating point is positioned at the maximum rotational speed and the chosen normalized design mass flow $\dot{m}_{cp,norm}$ (see Table 7).

4.2. Cooling system (stage 2)

The cooling system is sized with the known waste heat flows from stage 1. The inlet and outlet areas $A_{d,in}$ and $A_{d,out}$ of each diffuser are initially chosen based on the maximum heat flow $\dot{Q}_{max}$ of each cooling loop and an optimizable ratio $a = A/\dot{Q}_{max}$ (see Table 7). The normalized diffuser inlet area $a_{dr,in}$ determines the cooling air mass flow (see section 3.5). Hence, it can be used to trade a lower heat exchanger effectiveness and mass for a decreased cooling drag. The normalized outlet area $a_{dr,out}$ determines the heat exchanger frontal area $A_{hx,front,max} = A_{dr,out}$. This parameter can be used to trade a higher pressure recovery in the diffuser for a reduced frontal area of the heat exchanger. After sizing the heat exchangers based on section 3.3.3, the diffuser outlet areas are updated with the actual frontal areas of the three heat exchangers.

4.3. Postprocessing and design verification (stages 3 and 4)

At the beginning of stage 3, all system components are preliminarily sized. However, the approximations in stage 1 result in a larger compressor than needed. To determine the required compressor size more accurately, the preliminary system is simulated for each flight phase. The stack's current density for a required net power output $P_{sys,eff}$ is determined iteratively. Since the humidifier size is now fixed, both the stack inlet pressure $p_{stack,C,in}$ and relative humidity $RH_{stack,C,in}$ are chosen to maximize the overall system efficiency. The sizing process evaluates pressures between 1 and 2 bar abs. with 0.1 bar increments and humidities between 0 % and 100 % with 10 % increments. Pressures and humidities that cannot be achieved by the compressor and humidifier are detected and ignored. The interaction of the component models during the simulation of the overall system is shown in detail in Appendix E. After conducting the simulation for each flight phase, the compressor size is updated based on the more accurate maximum pressure ratio and mass flow. A smaller compressor results in a smaller outlet area of the diffuser for reactant air $A_{d,out,react} = A_{cp,in}$, which changes the compressor's inlet pressure. The compressor and diffuser sizing is repeated iteratively to resolve this circular dependence. The coolant pump size is updated based on the actual maximum hot side pressure drop of the fuel cell cooler. In stage 4, the fully sized system is simulated again to verify that all components are operated within their feasible operating range in each flight phase.

5. Results and discussion

5.1. Model validation

To assure that the developed system model is sufficiently accurate for the purpose of this study, the models for the stack, humidifier, heat exchanger and compressor are validated below. The remaining simpler component models are based on well-known thermodynamic principles (diffuser and nozzle) or are directly based on manufacturer data for existing components (coolant pump, anode recirculation blower).

5.1.1. Stack

The stack model is validated for varying current densities, cathode inlet pressures, air stoichiometric ratios and coolant temperatures. The effect of these operating parameters on the cell voltage is shown in Fig. 4. The figure shows the mean cell voltage of the Powercell S3 stack, which was measured with the test bench that is described in section 3.1.1. The corresponding operating conditions during the experiments are summarized in Table 8. The model is able to capture the effect of these different operating conditions with good accuracy. It should be

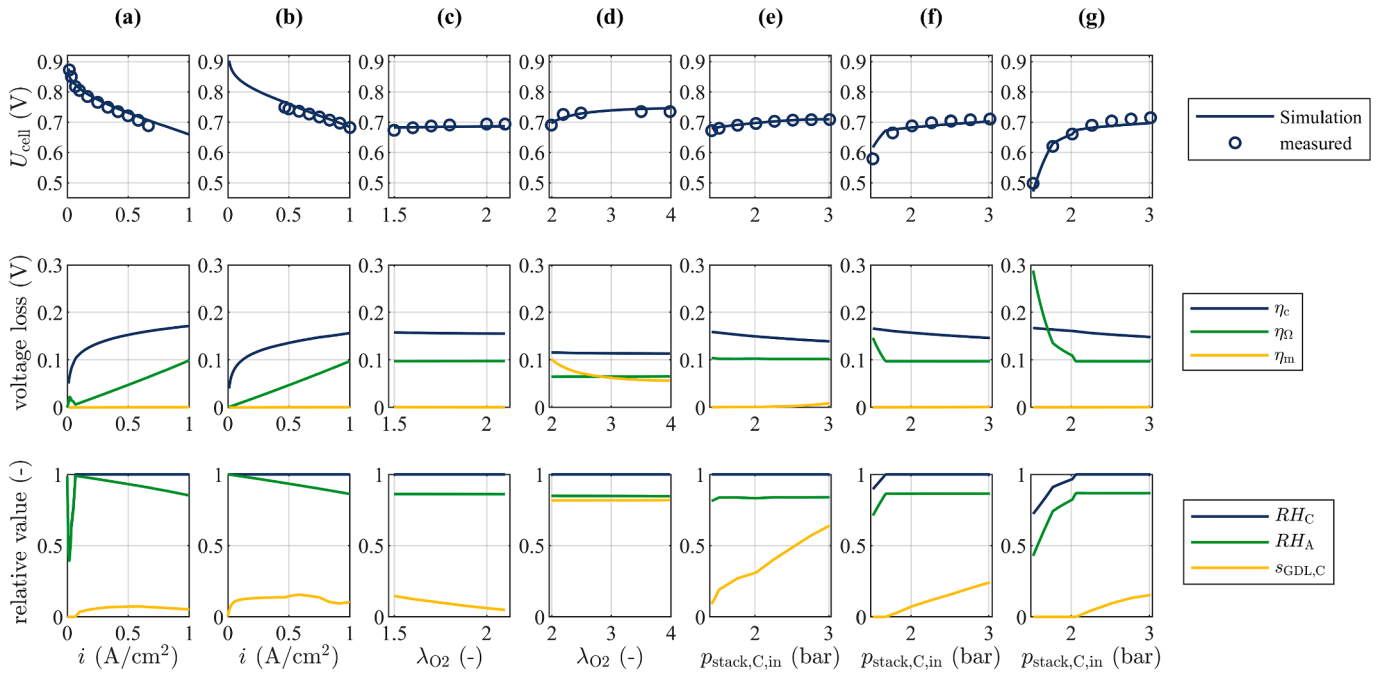

Fig. 4. Stack model validation. First row: simulated and measured average cell voltage in stack, second row: simulated activation loss η_c, ohmic loss η_Ω and mass transport loss η_m, third row: simulated humidity in cathode and anode control volumes RH_C and RH_A and saturation of cathode GDL with liquid water $s_{GDL,C}$ as defined in ref. [17]. The detailed conditions are provided in Table 8. (a) Variation of the current density at 1.1 bar (b) Variation of the current density at 2.0 bar (c) Variation of λ_{O_2} at 70 °C (d) Variation of λ_{O_2} at 28 °C (e) Variation of the pressure at 64 °C (f) Variation of the pressure at 78 °C (g) Variation of the pressure at 83 °C.

Table 8
Stack operating conditions in the experiments that are used for the model parameter fit and validation. $RH_{stack,C,in}$ is defined at the respective $T_{stack,C,in}$.

Parameter	Symbol	Fig. 4 (a)	Fig. 4 (b)	Fig. 4 (c)	Fig. 4 (d)	Fig. 4 **(e)**	Fig. 4 **(f)**	Fig. 4 **(g)**
Current density (A/cm^2)	i	varied	varied	1.0	0.5	1.0	1.0	1.0
Cathode stoichiometric ratio (-)	λ_{O_2}	1.8	1.8	varied	varied	1.8	1.8	1.8
Cathode inlet air pressure (bar abs.)	$p_{stack,C,in}$	1.1	2.0	2.0	2.0	varied	varied	varied
Coolant outlet temperature (°C)	$T_{stack,cw,out}$	68	72	70	28	64	78	83
Cathode inlet air relative humidity (-)	$RH_{stack,C,in}$	0.99 to 1	0.29 to 1	0.64 to 0.84	0.38 to 0.40	0.94 to 0.96	0.91 to 0.97	0.88 to 0.98
Cathode inlet air temperature (°C)	$T_{stack,C,in}$	38 to 55	31 to 39	33 to 34	27 to 32	34	34	35

noted that the stack model parameters were fitted with the same operating points in Fig. 4 that are used to validate the model.[1] These operating points capture a wide range of conditions and all fitted parameters are constrained to a plausible range (see section 3.1.2). Therefore, it is reasonable to assume that a model that is parameterized in this manner is indeed able to capture the underlying physical phenomena [38].

The effects of varying current densities during unpressurized and pressurized operation are shown in Fig. 4 (a) and (b). The experiments focused on moderate current densities of up to 1 A/cm^2 because this range is most relevant to aircraft applications [7,10]. Based on the simulation results, activation losses dominate in these operating points. Results for the operation at varying λ_{O2} with moderate (70 °C) and very low (28 °C) temperatures are shown in Fig. 4 (c) and (d). The simulations suggest that low temperatures in combination with low stoichiometries and low current densities (0.5 A/cm^2) result in moderate flooding of the cathode gas diffusion layer (GDL). This leads to increased mass transport losses at these conditions (see Fig. 4 (d)).

The effect of varying operating pressures at different temperatures is shown in Fig. 4 (e) to (g). Specifically, Fig. 4 (e) shows the effect of varying pressures at a constant temperature of 64 °C, Fig. 4 (f) at 78 °C and Fig. 4 (g) at 83 °C. The detailed conditions are given in Table 8. At 64 °C (Fig. 4 (e)), an increased operating pressure leads to a moderate increase in cell voltage because of decreased activation losses. At higher temperatures of 78 °C (Fig. 4 (f)) and 83 °C (Fig. 4 (g)), a more significant drop of the cell voltage is observed at pressures below about 1.5 bar. According to the simulated voltage losses, this decrease in cell voltage is a result of increased ohmic losses at these conditions (see Fig. 4 (e) to (g), second row).

5.1.2. Humidifier

Fig. 5 (a) and (b) show the validation of the humidifier model. The effect of the dry side air flow on the achievable approach-dew-point temperature ADT_{hm} is validated in Fig. 5 (a). According to measurements by Tallgren et al. [44], higher volume flows result in higher approach-dew-point temperatures. The model captures the trend and magnitude of this effect quite accurately. The operating conditions for the measurements by Tallgren et al. are $p_{hm,d,out} = 1.35$ bar, $p_{hm,w,in} = 1.35$ bar, $T_{hm} = 78$ °C, $T_{dew,d,in} = 20$ °C, $T_{dew,w,in} = 78$ °C [44] (nomenclature from section 3.2). These values were used as boundary conditions for the model validation in Fig. 5 (a). Note that the measured datapoint at $\dot{V}_{hm,d,in} = 1200$ L/min was used to fit the model parameters (see section 3.2.3). The assumption of a linear dependence of core volume and mass for different humidifier sizes is validated in Fig. 5 (b).

[1] Operating points with current densities below 0.3 A/cm^2 or air stoichiometries above 3.7 were excluded during model parameterization in order to improve the accuracy of the fit.

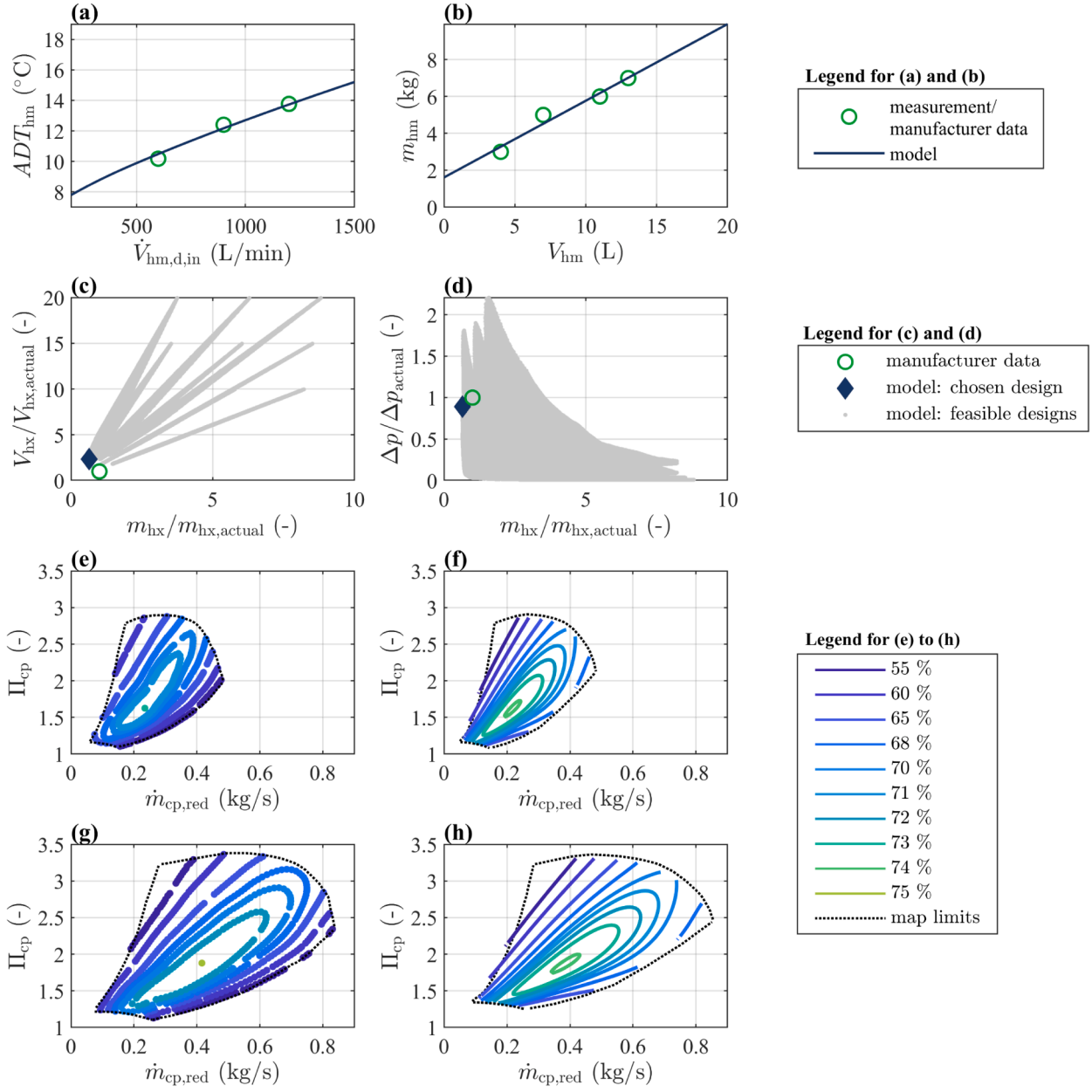

Fig. 5. Auxiliary component model validation. The reference conditions for the compressor maps in charts (e) to (h) are 15 °C and 1.013 bar [25]. (a) Humidifier: Effect of dry air volume flow on approach dew point temperature based on measurements by Tallgren et al. [44]. (b) Humidifier: Correlation of core volume and mass, manufacturer data from ref. [39] (c) Air-to-liquid heat exchanger: prediction of mass and volume (d) Air-to-liquid heat exchanger: prediction of mass and air side pressure drop (e) Compressor: efficiency map of C38-61 type, manufacturer data [25] (f) Compressor: prediction of scaled empirical model for C38-61 type (g) Compressor: efficiency map of C38R-112 type, manufacturer data [53] (h) Compressor: prediction of scaled empirical model for C38R-112 type.

Table 9
Manufacturer specifications for an air-to-liquid heat exchanger. The exact values are known to the authors but cannot be stated for confidentiality reasons.

Parameter	Value
Rated heat flow	63 kW
Rated hot side inlet temperature	65 °C
Rated cold side inlet temperature	30 °C
Rated effectiveness	0.4
Rated air-side pressure drop	<500 Pa
Heat exchanger mass	<10 kg
Heat exchanger volume	<30 L
Hot side fluid	50 % ethylene glycol/water mixture
Cold side fluid	Air
Fin surface type	Herringbone fin

5.1.3. *Heat exchanger*

The air-to-liquid heat exchanger model is validated with manufacturer data for a heat exchanger that was designed for DLR's Hy4 experimental aircraft [61]. This heat exchanger has similar temperature and pressure drop requirements, but the rated heat flow of 63 kW is lower than in the investigated 312 kW system (see Table 9). Data from the smaller heat exchanger is nevertheless suitable to validate the model, because the model is not limited to a specific heat exchanger size but instead determines the required size as an output. It should also be noted that the validation heat exchanger uses a different fin surface type than the model. However, by comparing the predicted heat exchanger size to an actual design, one can qualitatively validate both the modelling approach itself and the choice of fin surface.

The outputs of the sizing algorithm are compared to the

manufacturer specifications in Fig. 5 (c) and (d). As described in section 3.3.3, the sizing algorithm investigates a large number of geometric parameter combinations. Fig. 5 (c) and (d) show the combinations that fulfill the sizing requirements and highlight the design that is chosen by the sizing algorithm. The predicted mass, volume and pressure drop are reasonably close to the manufacturer data. Since the air-to-air heat exchanger model version makes use of the same fin surface as the air-to-liquid version, it can also be expected to be sufficiently accurate for the purpose of this study.

5.1.4. Compressor

The compressor model is based on three main approaches, namely the Mach number similarity concept, the Jensen-Kristensen model equations and the empirical scaling approach. The Mach number similarity concept is used to consider the effect of different altitudes on the compressor performance (see section 3.4.2). This concept is well-established in the literature [24,56,57] and has been comprehensively validated for a single-stage radial compressor by Schröter et al. [57]. The validation of the Jensen-Kristensen model equations and the empirical scaling approach is shown in Fig. 5 (e) to (h). These two approaches are validated by parameterizing the model based on a given compressor design and comparing the model's predictions for two different compressor sizes with manufacturer data [25,53]. Specifically, the performance of a smaller C38-61 compressor with a maximum mass flow of 0.48 kg/s and a larger C38R-112 compressor with a maximum mass flow of 0.84 kg/s are predicted using only datapoints from a C38-91 compressor (maximum mass flow of 0.63 kg/s). As shown in Fig. 5 (e) to (h), the efficiency data points of the two different compressors are predicted accurately by the scaled analytical model.

5.2. Fuel cell system sizing and simulation

After validating the component models, the system model is used to assess the performance of the propulsion unit for the investigated regional aircraft. Fig. 6 (a) to (c) show the aircraft's power requirement, altitude and air velocity throughout its design mission, which is provided by Atanasov [18]. The system sizing (stage 1 to 3 in Fig. 3) is conducted for seven representative flight phases that are highlighted in Fig. 6 (a). The simulation (stage 4 in Fig. 3) is conducted for the seven sizing points and 50 additional points, resulting in a total of 57 steady-state operating points throughout the mission profile.

5.2.1. Efficiency, drag and stack operating conditions

The simulated efficiencies are shown in Fig. 6 (d). A system efficiency $\eta_{\mathrm{sys,LHV}}$ of 49 % at takeoff and 39 % during cruise is observed. The resulting hydrogen consumption is 606.1 kg (for all 10 pods, not including reserves and unused boil-off). During descent ($t > 180$ min), $\eta_{\mathrm{sys,LHV}}$ drops significantly. The reason for this is the required bypass to avoid the compressor's surge limit (see section 5.2.2). However, this only has a small effect on the total hydrogen consumption because the power requirement is small in this flight phase.

The predicted cruise efficiency of 39 % is somewhat lower than in previous studies [7,11]. The main reason for the lower efficiency is that this work considers a higher cruise altitude of 8840 m. At high altitudes, the ambient pressure decreases and the compressor requires more auxiliary power. Abu Kasim et al. [7] calculated a cruise efficiency of around 47 % (converted to LHV-based value) for a lower flight altitude of around 3050 m. Sparano et al. [11] calculated an efficiency of around 53 % (converted to LHV-based value) but did not explicitly consider the effect of high altitudes on the system efficiency.

In combination with a typical efficiency of 94 % for large electric motors and 97 % for the power converter [54], the predicted fuel cell system efficiency results in an overall powertrain efficiency[2] between 36 % and 45 % (LHV-based, hydrogen flow to shaft power). This is higher than the efficiency of small turboprop engines for regional aircraft, but lower than the efficiencies of large turbofan engines. The reason for this is that the efficiency of gas turbines increases significantly for larger rated powers. For example, a T56 turboprop engine achieves efficiencies between 22 and 26 % (LHV-based, kerosene flow to shaft power) [62]. Large turbofan engines on the other hand achieve maximum efficiencies of up to 55 % (LHV-based, kerosene flow to shaft power) [8].

The drag that is caused by the different ram air streams is shown in Fig. 6 (e). It is found that the fuel cell cooler has by far the biggest contribution to the system's drag. The resulting total drag per pod is 476 N after takeoff and 333 N during cruise. For comparison, the aircraft design by Atanasov requires a thrust of about 2700 N per pod at takeoff [18]. The additional drag of the fuel cell system can therefore be expected to significantly penalize the aircraft's performance. A reduced drag could be achieved by reducing the system's waste heat via an improved efficiency or by increasing the stacks' operating temperature and thereby reducing the required cooling air mass flow. The power flows that are supplied by the stacks and consumed by the auxiliary components are shown in Fig. 6 (f). As expected, the compressor consumes the most auxiliary power while the contribution of the coolant pump and anode recirculation blowers is small.

The variation of stack operating conditions throughout the flight mission is shown in Fig. 6 (g) to (i). The current density varies according to the required stack power and stays below the chosen maximum value of $i_{\mathrm{des}} = 0.6\ \mathrm{A/cm^2}$ (see section 4). During descent, the current density drops as low as $0.03\ \mathrm{A/cm^2}$. Such a low current density is feasible but not ideal, since it can result in an accelerated degradation of the cells [63]. This could be avoided by only using several of the 10 pods in flight phases with a low power requirement.

The pressure and relative humidity are optimized for each flight phase according to section 4 and therefore vary based on the power requirement, altitude and air velocity. The optimization only considers relative humidities and pressures that can actually be achieved in the respective flight phase. During takeoff, the optimal cathode inlet pressure is 1.6 bar (abs). At the aircraft's cruise altitude of 8840 m, the ambient pressure drops to 0.31 bar (abs). In combination with the maximum pressure ratio of 3.38 of the investigated single-stage compressor [53], this limits the feasible cathode inlet pressure to 1.0 bar (abs) during cruise. Fig. 6 (i) shows the used and maximum feasible amount of humidification. During cruise, the amount of humidification is constrained by the chosen humidifier size. During takeoff, climb and descent, the optimal humidity is below the maximum feasible value and is therefore not constrained by the humidifier.

5.2.2. Compressor sizing

Fig. 7 shows the predicted compressor map based on the sizing approach from section 3.4.3 and highlights the 7 representative flight phases that are marked in Fig. 6 (a). All operating points are within the map limits, thereby confirming the initial assumption that one single-stage compressor can meet the mass flow requirements in all flight phases. During descent (phase 6 and 7), this is achieved by compressing more air than needed and bypassing the excess air, thereby shifting operating points 6′ and 7′ to the right side of the surge control limit [7].

5.2.3. System mass and volume

The resulting component sizes are shown in Fig. 8. The stacks are found to have the largest contribution to the overall mass, followed by the compressor and the humidifiers. The compressor's mass is mainly caused by the electric motor that drives the impeller, while the impeller

[2] Powertrain efficiency definition: $\eta_{\mathrm{shaft}} = P_{\mathrm{shaft}}/(\dot{m}_{\mathrm{fuel}} LHV_{\mathrm{fuel}})$

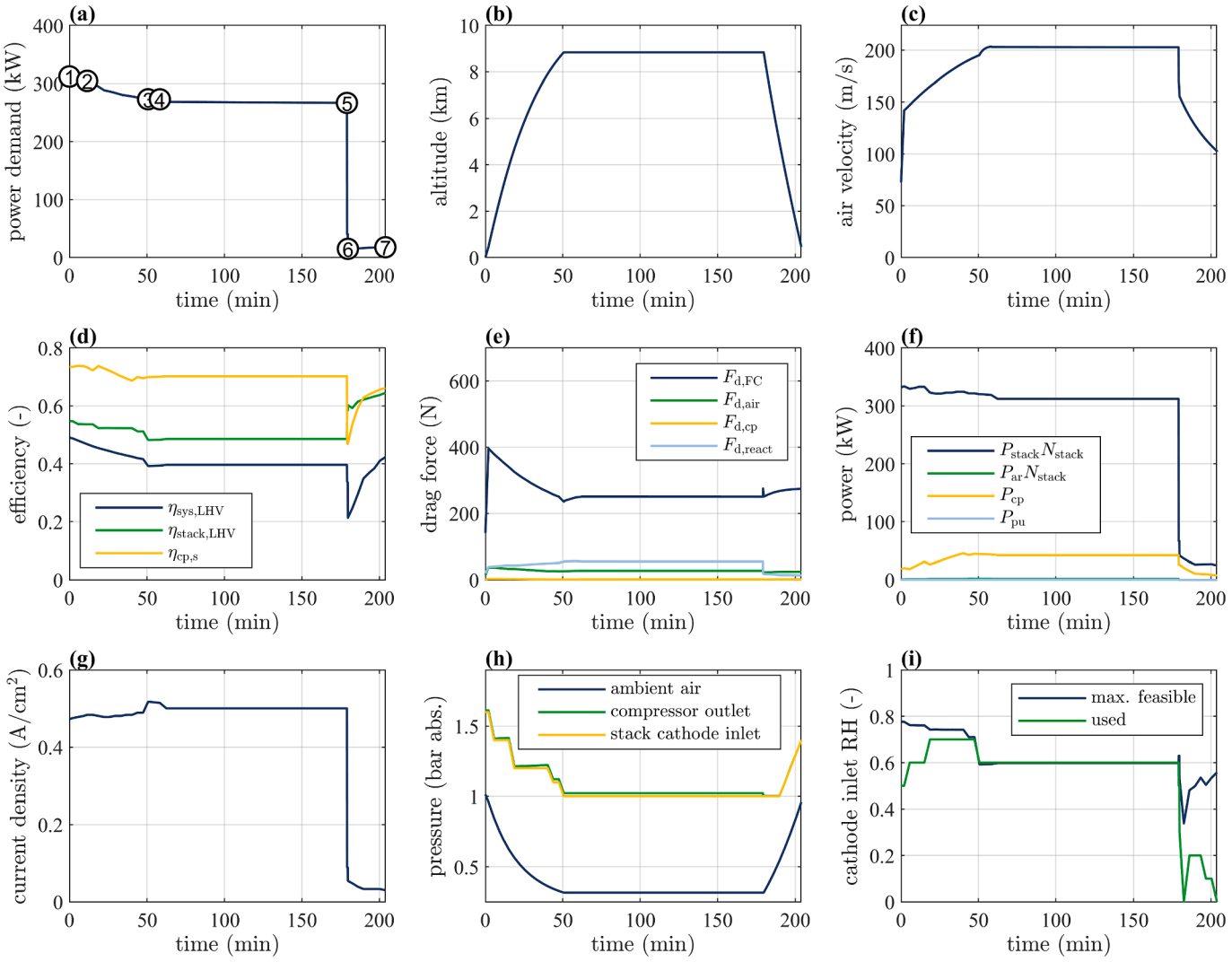

Fig. 6. System performance during the flight mission. (a) to (c) show inputs to the sizing and simulation, (d) to (i) show simulation results. All quantities are given for one of the ten pods. (a) net power requirement, sizing points highlighted with circles (b) altitude (c) air velocity at the inlet of the diffusers (d) efficiency of compressor $\eta_{cp,s}$, stack $\eta_{stack,LHV}$ and overall system $\eta_{sys,LHV}$ (e) drag force components as defined in section 2.1 (f) power flows (absolute values, sign according to Eq. (1)) (g) Stack current density (h) Pressures (i) Stack cathode inlet relative humidity, defined with $T_{fl,C,in} = 85$ °C

itself has a small contribution. The heat exchangers, coolant pump and anode recirculation blower are of minor importance in terms of mass and volume.

Without the cooling system, the system's predicted specific power is 0.54 kW/kg (defined with the max. power output at sea level). This is comparable to manufacturer specifications for an existing fuel cell system by Powercell that uses the same stack technology and achieves 0.47 kW/kg (without the cooling system) [64]. The predicted power density of 0.48 kW/L is somewhat higher than the Powercell system (0.35 kW/L) [64]. This is the case because the volume of wiring, piping and several smaller auxiliary components is not considered by the model (see section 2.1). The properties of several other fuel cell systems for ground-based applications are summarized in Table 10. These systems are based on different fuel cell stacks and achieve somewhat lower specific powers. A possible explanation is that these systems are developed for heavy-duty applications. Hence, they are not necessarily optimized for a high specific power.

When including the cooling system, the model predicts a specific power of 0.50 kW/kg and a power density of 0.39 kW/L. This result is within the range of values in previous studies [7,11]. As described in section 2.1, the predicted specific power of 0.50 kW/kg excludes the mass of wires, piping and air inlets. The power converters, battery storage and the electric motor that drives the propeller further increase the overall powertrain mass. Overall, this results in a much heavier propulsion system than in existing aircraft. For comparison, the PW127 turboprop engine that is used in ATR72 regional aircraft achieves about 4.27 kW/kg and > 1.74 kW/L [67]. The fuel cell system's specific power would need to increase significantly to be competitive to conventional aircraft engines. This goal is also outlined in recent development roadmaps for fuel cell systems in aviation: The EU's Strategic Research and Innovation Agenda targets a specific power of 2.0 kW/kg by the year 2030 (including the cooling system) [68]. Similarly, the United Kingdom's FlyZero project set a target of 2.0–2.5 kW/kg by 2030 and 3.0–3.5 kW/kg by 2050 (including the cooling system) [69].

According to Fig. 8, the most substantial improvement could be achieved by decreasing the mass of the stacks, compressor motor and humidifier. A promising approach to decrease the stack mass is to increase the power output per active cell area (W/m^2), for example with enhanced catalyst layers [70]. Another way to increase the stack's specific power is to reduce the cell mass per active cell area (kg/m^2), for example by using a weight-optimized cell design and titanium bipolar plates [15]. The mass of the compressor motor could be reduced by increasing the motor's specific power via improved motor designs and materials [71]. Another option would be to reduce the installed motor

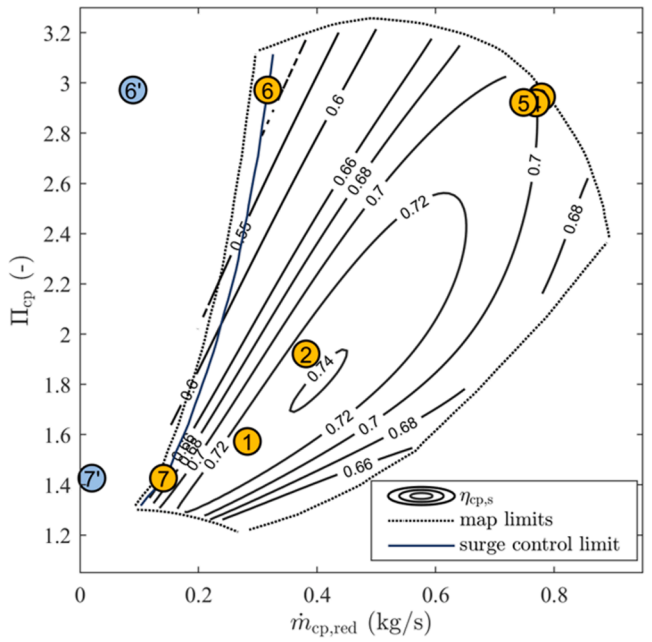

Fig. 7. Compressor map for the investigated 312 kW system. Flight phases that were used for sizing the system are highlighted with circles, the phases are numbered according to Fig. 6 (a).

power by adding a turbine to the compressor shaft (see section 2). The mass of the humidifier may be reduced via mass-optimized designs (the investigated membrane humidifiers are currently optimized for a low volume [39]), or by using different membrane materials with a higher permeability.

Besides the mass and volume of the fuel cell system, there are a number of additional factors that determine whether fuel cells could become a competitive option for the propulsion of regional aircraft. On the one hand, the volumetric energy density of liquid hydrogen (8.5 MJ/L) is about 4 times lower than that of conventional jet fuel (34.9 MJ/L) [2]. The gravimetric energy density of hydrogen (120 MJ/kg) is higher than that of jet fuel (43.2 MJ/kg), but the liquid hydrogen tank will be several times heavier than the hydrogen that it contains [2,11]. On the other hand, fuel cells would require less fuel than a turboprop engine because of their higher efficiency (see section 5.2.1). Moreover, their scalability enables distributed propulsion which can potentially further reduce the aircraft's fuel consumption [2,20]. Ultimately, the feasibility of fuel cells for regional aircraft propulsion will need to be assessed at the overall aircraft level and does not only depend on the performance of the propulsion system.

5.2.4. *Model accuracy and limitations*

The model's accuracy and its limitations can be summarized as follows. The size of the stacks and humidifiers are based on detailed and

Table 10
Manufacturer specifications of existing fuel cell systems for ground-based applications. The values for specific power and power density do not include the cooling system. The examples were chosen because the performance of these systems is publicly known. There are a number of additional manufacturers that do not publish the detailed performance of their fuel cell systems.

Manufacturer, Type	Net power output	Specific power	Power density
Powercell Sweden AB, P System 100 [64]	100 kW	0.47 kW/kg	0.35 kW/L
Plug Power Inc., ProGen module [65]	125 kW	0.34 kW/kg	0.31 kW/L
Nuvera Fuel Cells LLC., E-60-HD [66]	59 kW	0.31 kW/kg	0.20 kW/L

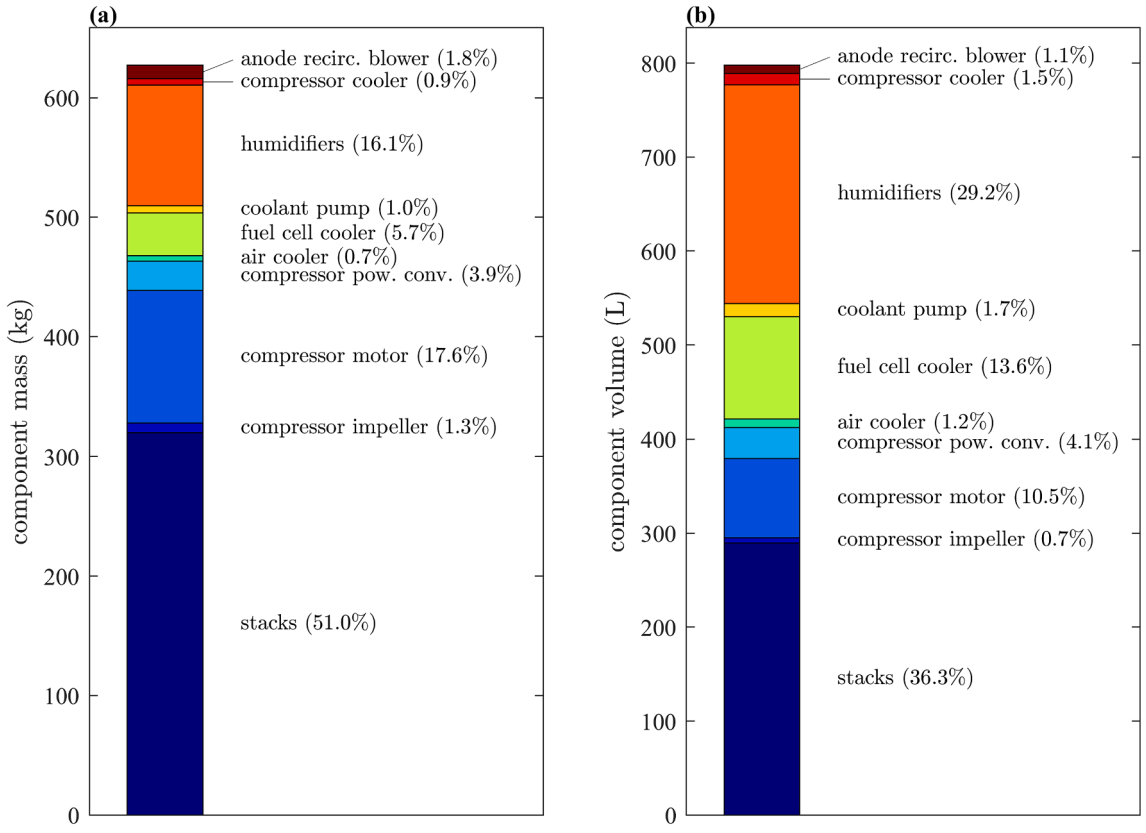

Fig. 8. Sizing result for the investigated 312 kW system. (a) mass of components in one pod, (b) volume of components in one pod.

validated models. The predictions for these components can therefore be assumed to be quite accurate. The heat exchanger model was validated with manufacturer data, but is based on a simplified 1D geometry. The predicted mass might change if the heat exchanger geometries would be considered with a 2D or 3D model. The assumption for the compressor size is that the mass and volume scale linearly with the required mass flow (see section 3.4.3). This linearization provides accurate results as long as the required mass flow is reasonably close to the rated mass flow of the baseline design. A higher uncertainty can be expected for the coolant pump and anode recirculation blower, because these components are considered with simpler models. However, this only has a small impact on the predicted system performance: For example, even if the predicted coolant pump mass would be off by 50 % (9.20 kg instead of 6.13 kg), the overall system mass would only increase by 0.5 % (see Fig. 8). The same argument holds true for the predicted system efficiency: The power share of the coolant pump and anode recirculation blower is much smaller than that of the stacks and compressor (see Fig. 6 (f)). For the system's drag, a source of uncertainty is the assumed diffuser and nozzle efficiency. A more detailed assessment of the efficiencies of the diffuser and nozzle would require a detailed computational fluid dynamics (CFD) model or experimental data from an existing prototype.

5.3. Pareto-optimal system design

Section 4 introduced a number of design parameters that can be used to optimize different aspects of the fuel cell system performance. The system design in section 5.2 was carried out for one set of these parameters (see Table 7). This section examines how these parameters can be chosen to achieve different design targets such as a low mass m_{sys}, high overall efficiency $\eta_{\mathrm{sys,LHV}}$, low drag $F_{\mathrm{d,tot}}$ and low volume V_{sys}. Such a tradeoff between multiple contradicting design targets can be viewed as a pareto (multi-objective) optimization problem:

$$\underset{\mathbf{k}}{\text{minimize}} \left(m_{\mathrm{sys}}(\mathbf{k}), -\eta_{\mathrm{sys,LHV}}(\mathbf{k}), F_{\mathrm{d,tot}}(\mathbf{k}), V_{\mathrm{sys}}(\mathbf{k}) \right)$$

The objective function of this optimization problem is given implicitly by the sizing process and the underlying Eqs. (1) to (61). The vector $\mathbf{k} = [i_{\mathrm{des}}, RH_{\mathrm{des}}, a_{\mathrm{FC,in}}, a_{\mathrm{FC,out}}]$ contains the optimizable design parameters that were introduced in section 4. The feasibility of a combination of design parameters $\mathbf{k}$ is evaluated during the system sizing process. This optimization problem could be solved by scalarizing the above vector-valued objective function with weighting factors $w_1,\ldots,w_4$.

$$f_s = w_1 m_{\mathrm{sys}} + w_2 \eta_{\mathrm{sys,LHV}} + w_3 F_{\mathrm{d,tot}} + w_4 V_{\mathrm{sys}}$$

The resulting objective function f_s can then be minimized with any suitable optimization algorithm, for example with a genetic algorithm. Appropriate weighting factors can only be determined at the overall aircraft level, since additional effects such as aerodynamics, cost and structural design of the fuselage, wings and tank need to be considered.

Here, we do not solve the above optimization problem explicitly but instead explore the underlying trends in a more general way. This is done by repeating the sizing process for different combinations of design parameters $\mathbf{k}$ and assessing the changes to the fuel cell system performance. To achieve a feasible computation time, the analysis is limited to the four parameters i_{des}, RH_{des}, $a_{\mathrm{FC,in}}$ and $a_{\mathrm{FC,out}}$. These parameters were selected because they affect the most relevant system components (which were identified in section 5.2):

- The rated current density i_{des} determines the stack's mass and efficiency.
- The constraint for the humidity at the stack's cathode inlet RH_{des} determines the humidifier size and stack efficiency.
- The diffuser areas $a_{\mathrm{FC,in}}$ and $a_{\mathrm{FC,out}}$ determine the drag of the fuel cell cooler.

The remaining design parameters from Table 7 are kept constant in this section, because they affect the design of less relevant system components: The hot side pressure drop of the heat exchangers affects the mass of the heat exchangers, but the heat exchanger mass is small in the overall system context (see Fig. 8). The drag is only affected by the cold side pressure drop, which is indirectly determined by the diffuser areas. The design parameter $\dot{m}_{\mathrm{cp,norm}}$ affects the compressor efficiency throughout the different flight phases. However, because the efficiency does not vary drastically in the upper region of the compressor map (see Fig. 7), $\dot{m}_{\mathrm{cp,norm}}$ only has a moderate effect on the overall system performance. The compressor mass and volume are independent of $\dot{m}_{\mathrm{cp,norm}}$, because they are determined directly from the required mass flow (see Eqs. (58) and (59)). The areas of the diffusers for the air cooler and compressor cooler are kept constant, because these components contribute much less to the overall drag (see Fig. 6 (e)).

The chosen range and resolution for the four considered design parameters are given in Table 7. The investigated range is chosen to capture a large fraction of the feasible design space. The limits of the feasible design space were approximated by manually testing different parameter combinations. The chosen resolution results in 252 combinations that are being evaluated. 162 out of the investigated combinations lead to feasible designs. Infeasible designs can occur for some combinations of diffuser inlet and exit areas: If the inlet area $a_{\mathrm{FC,in}}$ is set too low, the incoming air mass flow becomes too small to remove the stack's waste heat. Additionally, if the diffuser outlet area $a_{\mathrm{FC,out}}$ is set too low, the pressure increase in the diffuser becomes small (see section 3.5). This can prevent the heat exchanger sizing from converging, because the constraint for the cold side pressure drop cannot be met (see section 3.3.3).

The mass, volume, efficiency and drag of the 162 feasible designs are compared in Fig. 9. The efficiency and drag vary throughout the flight mission and could be optimized for any given flight phase with the developed approach. In this section we focus on the performance in the cruise phase (point 4 in Fig. 6) because this flight phase has the largest effect on the overall hydrogen consumption. The results in Fig. 9 (a) show that different combinations of design parameters lead to a wide range of masses and efficiencies. The design (B) with the highest efficiency (43 %) is also the heaviest, while design (A) achieves a 19 % lower mass in combination with a lower efficiency (38 %). The drag of the different designs varies even more significantly, with the best case having 75 % less drag than the worst case. Because different choices of the diffuser inlet and outlet areas $a_{\mathrm{FC,in}}$ and $a_{\mathrm{FC,out}}$ have a strong effect on the system's drag but do not change the model result for the system mass (see section 2.1), no clear correlation between mass and drag is observed. In terms of volume, heavier designs are found to generally also result in a larger volume.

Detailed properties of the selected designs (A) to (E) are given in Table 11. Interestingly, the design with the lowest mass is achieved with a moderate current density of 0.6 $\mathrm{A/cm^2}$ even though the investigated stack can be operated at much higher current densities (see Fig. 4 (b)). This is due to the fact that higher current densities lead to a decreased stack efficiency, which in turn leads to larger auxiliary components for the same net power output. Fig. 10 illustrates this effect in more detail. The graph shows the detailed mass breakdown for 5 points from Fig. 9. The design parameters RH_{des}, $a_{\mathrm{FC,in}}$ and $a_{\mathrm{FC,out}}$ are kept constant at the values for design (A), while the rated current density is varied between 0.5 and 0.9 $\mathrm{A/cm^2}$. It is found that the positive effect of a decreased stack mass is diminished by the larger mass of the auxiliary components, most notably an increased humidifier mass. Consequently, in terms of system mass there is no benefit of operating the stacks at current densities above 0.6 $\mathrm{A/cm^2}$ in the investigated case. The mass-optimal current density depends on the combined behavior of the stacks and auxiliary components. Hence, a different optimum value might be observed if a different stack type or different auxiliary components are used.

Only optimizing for efficiency leads to a heavy and voluminous

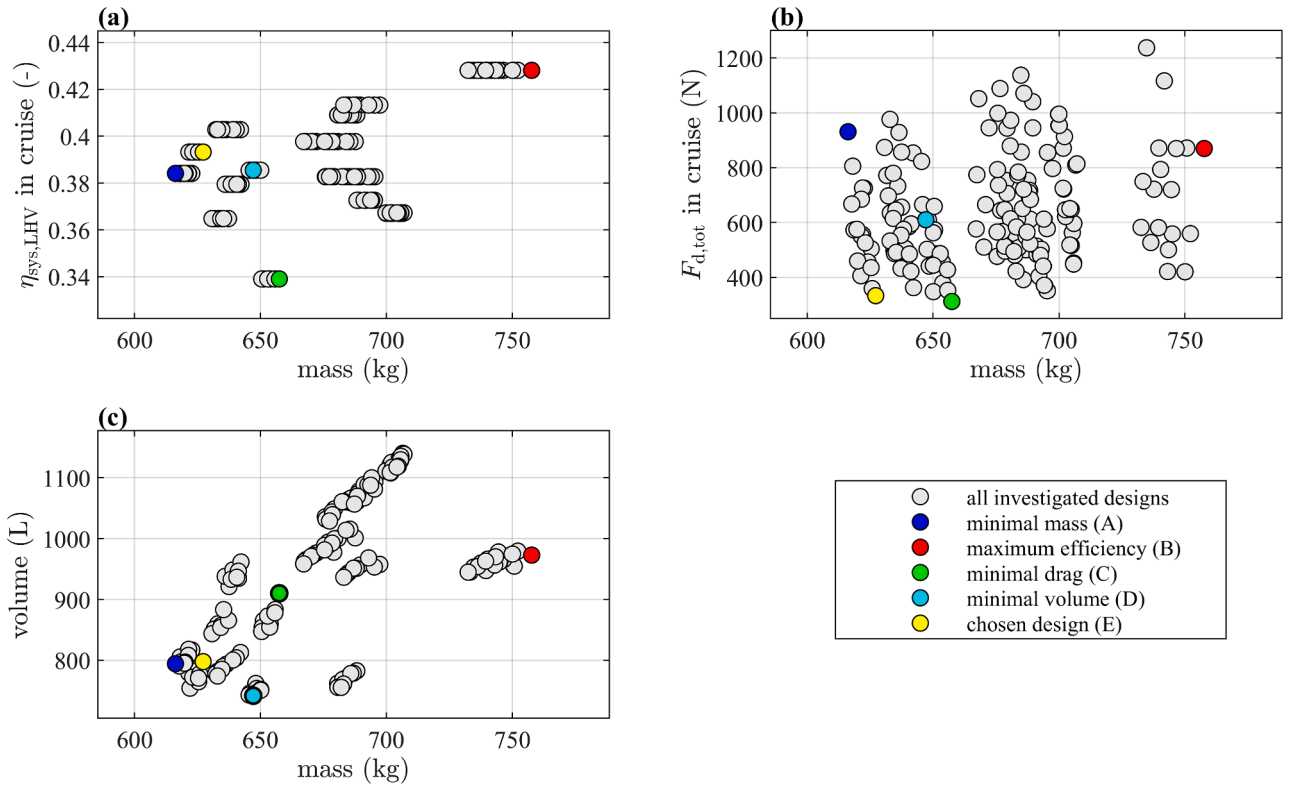

Fig. 9. Effect of the investigated design parameters on the fuel cell system performance. All quantities are given for one of the ten pods. (a) to (c) show the same designs in terms of different performance indicators. (a) Cruise efficiency $\eta_{sys,LHV}$ and mass m_{sys} (b) Cruise drag $F_{d,tot}$ and mass m_{sys} (c) Volume V_{sys} and mass m_{sys}

Table 11
Results for the fuel cell system designs that are highlighted in Fig. 9. All quantities are given for one of the ten pods.

Parameter	Symbol	Lowest mass (A)	Highest efficiency (B)	Lowest drag (C)	Lowest volume (D)	Chosen design (E)
Current density at the system's rated load (A/cm^2)	i_{des}	0.6	0.4	0.7	0.5	0.6
Constraint for max. relative humidity at the stack's cathode inlet (-)	RH_{des}	0.6	0.8	0.5	0.5	0.5
Inlet area of diffuser for main fuel cell cooler, normalized with waste heat (m^2/W)	$a_{FC,in}$	$5.28 \cdot 10^{-7}$	$4.32 \cdot 10^{-7}$	$4.32 \cdot 10^{-7}$	$5.28 \cdot 10^{-7}$	$4.32 \cdot 10^{-7}$
Outlet area of diffuser for main fuel cell cooler, normalized with waste heat (m^2/W)	$a_{FC,out}$	$3.76 \cdot 10^{-6}$	$3.76 \cdot 10^{-6}$	$4.60 \cdot 10^{-6}$	$4.18 \cdot 10^{-6}$	$4.60 \cdot 10^{-6}$
System mass (kg)	m_{sys}	616.25	757.67	657.51	647.17	627.24
System efficiency in cruise phase (-)	$\eta_{sys,LHV}$	0.38	0.43	0.34	0.39	0.39
Drag force in cruise (N)	$F_{d,tot}$	930.97	869.83	312.20	610.22	333.44
System volume (L)	V_{sys}	794.34	972.74	910.04	741.77	797.78
Max. power output at sea level (kW)	$P_{sys,eff}$	312.02	312.02	312.02	312.02	312.02
Inlet area of diffuser for main fuel cell cooler (m^2)	$A_{FC,in}$	0.19	0.13	0.21	0.20	0.18
Outlet area of diffuser for main fuel cell cooler (m^2)	$A_{FC,out}$	1.35	1.12	2.17	1.52	1.88

system (see design (B) in Fig. 9 (a) and Table 11). In this case, the stacks are operated at a low rated current density i_{des} and the humidifier is sized for a high amount of humidification. Moreover, only optimizing the overall efficiency does not automatically result in the lowest drag (see Fig. 9 (b)). This is the case because the diffuser inlet and outlet areas as well as the pressure drop in the heat exchangers significantly affect the drag but have no direct effect on the system efficiency. The design (C) with the lowest internal drag has a similar mass as design (A) but a decreased efficiency. Design (E) is the one that is discussed in detail in the previous section 5.2. It was selected because it achieves a good compromise in terms of mass and drag (see Fig. 9 (b)) and also performs well in terms of efficiency and volume.

6. Conclusions

This work investigated the design and optimization of a 312 kW fuel cell system for the propulsion of a regional aircraft. Detailed models for the fuel cell stacks, humidifier, heat exchanger and compressor were developed and validated. The models were coupled with a novel sizing approach that finds the smallest feasible combination of components while optimizing the stack's operating pressure and cathode inlet relative humidity for each flight phase. This sizing process was repeated for different combinations of design parameters to assess a wide range of possible system designs with respect to their mass, efficiency, drag and volume.

The key findings can be summarized as follows:

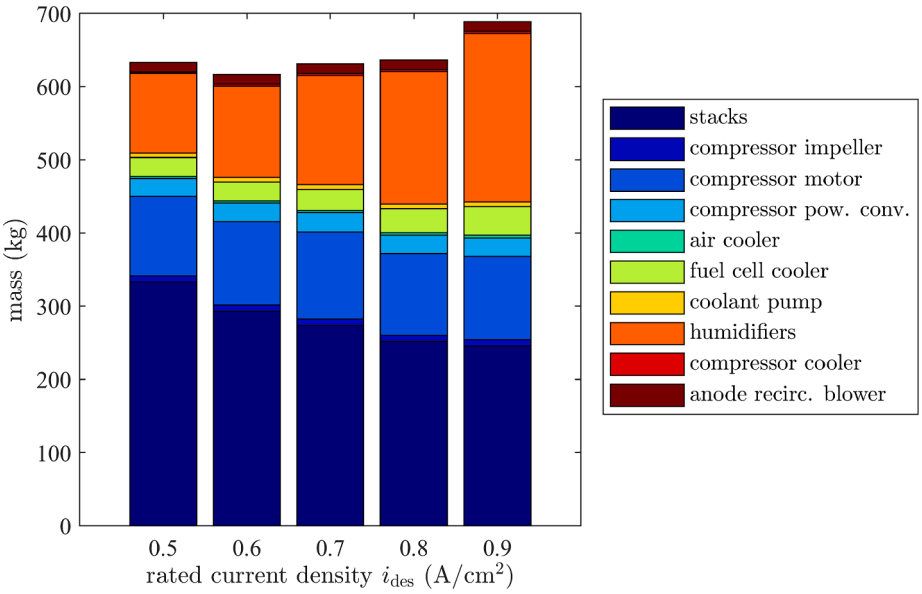

Fig. 10. Effect of the chosen rated current density i_{des} on the overall system mass.

(1) The results suggest that the design of fuel cell systems should be viewed as a pareto optimization problem where all relevant performance aspects are considered simultaneously. In the case of aircraft propulsion, the relevant technical performance aspects are mass, efficiency, drag and volume. The developed sizing approach enables pareto-optimal designs that perform well for all these performance aspects simultaneously. It is shown that if only some of the aspects would be optimized (e.g. mass and efficiency), the system would perform poorly in other aspects (e.g. drag).

(2) The performance of the 312 kW fuel cell system was analyzed based on state-of-the-art stacks and auxiliary components. The system is predicted to achieve an efficiency of 39 % during cruise and 49 % on ground (based on the lower heating value of hydrogen). The calculated cruise efficiency based on the detailed model is lower than previous estimates. The system's predicted specific power and power density are 0.50 kW/kg and 0.39 kW/L, these values are within the range of previous estimates. The drag during the cruise phase is 333 N. Compared to conventional turboprop engines for regional aircraft, the use of fuel cells leads to an improved propulsion system efficiency with the drawback of an increased mass and drag.

(3) The system mass and volume are mainly affected by the stacks, humidifier and the electric motor that drives the air compressor. The contribution of the cooling system to the overall mass and volume is small, but the drag that is caused by the cooling system significantly penalizes the aircraft's performance.

(4) Operation at higher current densities generally leads to a decreased stack mass for a given power output. However, it is not beneficial in terms of overall system mass to operate the stacks at current densities above 0.6 A/cm^2 in the investigated case. The reason for this is that the stack efficiency decreases with increasing current densities. Above 0.6 A/cm^2, the positive effect of a decreased stack mass is diminished by an increased mass of the auxiliary components due to the lower stack efficiency.

Future work will be directed at coupling the developed fuel cell system model to the overall aircraft design process. Ultimately, this will enable a detailed comparison with other technology options such as hydrogen combustion, synthetic kerosene, other fuel cell technologies and battery-hybrid concepts.

CRediT authorship contribution statement

Matthias Schröder: Writing – original draft, Software, Methodology, Investigation, Formal analysis, Conceptualization. **Florian Becker:** Writing – review & editing, Investigation. **Christoph Gentner:** Writing – review & editing, Supervision.

Declaration of competing interest

The authors declare that they have no known competing financial interests or personal relationships that could have appeared to influence the work reported in this paper.

Data availability

The heat exchanger validation data in section 5.1.3 is confidential, approximate values are provided in Table 9. The remaining data will be made available on request.

Acknowledgements

This work was supported by the Federal Ministry for Digital and Transport of Germany via Projektträger Jülich and NOW GmbH (research project number 03B10704) and by the Federal Ministry for Economic Affairs and Climate Action of Germany via DLR Projektträger (research project number 20M1909B, LuFoVI-1). The authors thank Gema Montaner Ríos, Anna Vorndran, Leonard Engel and Igor Sokolov for their support with the fuel cell test bench and Georgi Atanasov from DLR's Institute of System Architectures in Aeronautics for providing the aircraft concept.

Appendix A. Stack model details

The stack model is explained in detail in an earlier publication [17]. Its input and output variables are summarized in Table A.1. The bounds that were used when fitting the model parameters are provided in Table A.2.

Table A.1
Summary of stack model variables.

Parameter	Symbol	Type during sizing	Type during simulation
Cathode inlet pressure (Pa)	$p_{\text{stack,C,in}}$	Input	Input
Cathode inlet temperature (K)	$T_{\text{stack,C,in}}$	Input	Input
Cathode inlet relative humidity (-)	$RH_{\text{stack,C,in}}$	Input	Input
Cathode stoichiometric ratio (-)	λ_{O_2}	Input	Input
Cathode pressure drop (Pa)	$\Delta p_{\text{stack,C}}$	Output	Output
Anode inlet pressure (Pa)	$p_{\text{stack,A,in}}$	Input	Input
Anode inlet temperature (K)	$T_{\text{stack,A,in}}$	Input	Input
Anode inlet relative humidity (-)	$RH_{\text{stack,A,in}}$	Input	Input
Anode stoichiometric ratio (-)	λ_{H_2}	Input	Input
Coolant outlet temperature (K)	$T_{\text{stack,cw,out}}$	Input	Input
Current density (A/m^2)	i	Input	Output
Cell voltage (V)	U_{cell}	Output	Output
Required air mass flow (kg/s)	$\dot{m}_{\text{stack,C,in}}$	Output	Output
Required hydrogen mass flow (kg/s)	$\dot{m}_{\text{stack,A,in}}$	Output	Output
Required coolant mass flow (kg/s)	$\dot{m}_{\text{stack,cw}}$	Output	Output
Mass flow in anode recirculation loop (kg/s)	$\dot{m}_{\text{stack,ar}}$	Output	Output
Coolant pressure drop (Pa)	$\Delta p_{\text{stack,cw}}$	Output	Output

Table A.2
Fitted parameters of the fuel cell stack model. Nomenclature according to detailed model description in ref. [17].

Parameter	Symbol	Lower bound	Upper bound	background
Reference exchange current density (A m^{-2})	$i_{0,\text{ref}}$	10^{-1}	10^{3}	assumed
Reference limit current density (A m^{-2})	$i_{\text{lim,ref}}$	10^{4}	10^{8}	assumed
Cathode transfer coefficient (−)	α_{C}	0.2	1	based on [72]
Factor for spatial variation of temperature in channel (−)	c_{T}	0.55	0.95	based on [73]
Factor for spatial variation of relative humidity in channel (−)	c_{H}	0.5	1.5	assumed
Exponent for relative permeability (−)	n_{k}	2	5	based on [74]
Combined GDL-specificparameters (m^{-1})	c_{D1}	-10^{11}	-10^{6}	assumed
switch parameter in flooding sub-model (−)	q_{sw}	1	5	assumed
Effective GDL thickness (m)	$\delta_{\text{GDL,eff}}$	$1.1{\cdot}10^{-4}$	$2.5{\cdot}10^{-3}$	based on [75–77]
Coefficient in cathode pressure drop correlation, Eq. (8) (Pa/(kg/s))	k_{pC}	0	10^{10}	assumed

The stack model is extended with a heat balance for the stack.

$$\dot{Q}_{\text{cw}} = \dot{Q}_{\text{pro}} - \dot{Q}_{\text{C,evap}} - \dot{Q}_{\text{A,fl}} - \dot{Q}_{\text{C,fl}} \tag{A.1}$$

$$\dot{Q}_{\text{pro}} = N_{\text{cell}} i A_{\text{cell}} (U_{\text{th}} - U_{\text{cell}}) \tag{A.2}$$

$$\dot{Q}_{\text{C,evap}} = \dot{m}_{\text{H}_2\text{O,C,evap}} \Delta h_{\text{evap,H}_2\text{O}} \tag{A.3}$$

$\dot{Q}_{\text{cw}}$ is the waste heat flow that is removed by the liquid coolant, $\dot{Q}_{\text{pro}}$ is the produced heat if all water is in liquid form and $U_{\text{th}} = 1.48$ is the thermoneutral voltage [72]. The term $\dot{Q}_{\text{C,evap}}$ accounts for the evaporation of water within the stack. The mass flow of evaporating water $\dot{m}_{\text{H}_2\text{O,C,evap}}$ is determined by the stack model; $\Delta h_{\text{evap,H}_2\text{O}}$ is the evaporation enthalpy of water. The terms $\dot{Q}_{\text{A,fl}}$ and $\dot{Q}_{\text{C,fl}}$ account for temperature changes of the reactants within the stack.

$$\dot{Q}_{\text{A,fl}} = \dot{m}_{\text{stack,A,in}} c_{\text{p,H}_2} (T_{\text{stack,A,out}} - T_{\text{stack,A,in}}) \tag{A.4}$$

$$\dot{Q}_{\text{C,fl}} = \dot{m}_{\text{stack,C,in}} c_{\text{p,air}} (T_{\text{stack,C,out}} - T_{\text{stack,C,in}}) \tag{A.5}$$

The model assumes $T_{\text{stack,A,out}} = T_{\text{stack,cw,out}}$ and $T_{\text{stack,C,out}} = T_{\text{stack,cw,out}}$. The required coolant mass flow is

$$\dot{m}_{\text{stack,cw}} = \frac{\dot{Q}_{\text{cw}}}{c_{\text{p,cw}} (T_{\text{stack,cw,out}} - T_{\text{stack,cw,in}})} \tag{A.6}$$

where $T_{\text{stack,cw}}$ denotes the temperature at the stack's inlet and outlet and $c_{\text{p,cw}}$ is the specific heat capacity. The pressure drop of the coolant in the stack's coolant channels is approximated with the empirical correlation

$$\Delta p_{\text{stack,cw}} = k_{\text{pcw1}} \left(\frac{\dot{m}_{\text{stack,cw}}}{N_{\text{cell}}} \right)^2 + k_{\text{pcw2}} \left(\frac{\dot{m}_{\text{stack,cw}}}{N_{\text{cell}}} \right) \tag{A.7}$$

where the coefficients k_{pcw1} and k_{pcw2} are fitted to the experimental data that was recorded during the stack characterization.

Appendix B. Heat exchanger model details

Geometric parameters that serve as inputs when sizing the heat exchangers are listed in Table B.1. A detailed definition of these parameters is given by Chang et al. [49] (the same nomenclature is used here, the model considers type "C"). Additional geometric properties are calculated with the equations in Table B.2.

Based on Ref. [47], the air-to-liquid and air-to-air heat exchangers are designed to have cold layers (C) on the outside of the core and hot layers (H) in between those, which results in a "CHCH…HCHC" arrangement. Moreover, the fins of the two outer cold layers are designed to have half the fin length as those of the inner layers, so that their behavior approximately equals that of the cold layer in a symmetrical (…HCH…) set of inner layers. Under these assumptions, thermal symmetry can be assumed and no additional banking factor is needed to account for a different behavior of the two outer layers.

Table B.1
Summary of the independent geometric parameters in the heat exchanger model.

Parameter	Symbol	Lower bound	Upper bound	Number of discrete points
Parameters for validation case (air-to-liquid)				
Number of fin segments (-)	n_{fin}	10^4	10^5	200
Fin depth (mm)	F_d	40	80	90
Fin length (mm)	F_l	5	19	30
Fin pitch (mm)	F_p	1.1	2.2	3
Fin thickness (mm)	F_t	0.06	0.16	3
Louver pitch (mm)	L_p	1	1.86	3
Louver angle (°)	Θ	35	35	1 (not optimized)
Tube major diameter (mm)	D_m	1.5	1.5	1 (not optimized)
Tube wall thickness (mm)	T_t	0.06	0.06	1 (not optimized)
Parameters for full-scale system sizing (air-to-liquid)				
Number of fin segments (-)	n_{fin}	10^4 for FC cooler, 10^3 for compressor cooler	10^5	200
Fin depth (mm)	F_d	16	80	90
Fin length (mm)	F_l	5	19	30
Fin pitch (mm)	F_p	1.1	2.2	3
Fin thickness (mm)	F_t	0.06	0.16	3
Louver pitch (mm)	L_p	1	1.86	3
Louver angle (°)	Θ	35	35	1 (not optimized)
Tube major diameter (mm)	D_m	5	5	1 (not optimized)
Tube wall thickness (mm)	T_t	1	1	1 (not optimized)
Parameters for full-scale system sizing (air-to-air)				
Number of cold side fin segments (-)	$n_{fin,c}$	10^2	10^4	300
Cold side fin length (mm)	$F_{l,c}$	8	19	9
Cold side fin pitch (mm)	$F_{p,c}$	1.2	2.2	2
Cold side fin thickness (mm)	$F_{t,c}$	0.16	0.16	1 (not optimized)
Cold side louver pitch (mm)	$L_{p,c}$	1.3	1.3	1 (not optimized)
Cold side louver angle (°)	Θ_c	30	30	1 (not optimized)
Number of hot side fin segments (-)	$n_{fin,h}$	10^2	10^4	300
Hot side fin length (mm)	$F_{l,h}$	8	19	9
Hot side fin pitch (mm)	$F_{p,h}$	1.2	2.2	1
Hot side fin thickness (mm)	$F_{t,h}$	0.16	0.16	1 (not optimized)
Hot side louver pitch (mm)	$L_{p,h}$	1.3	1.3	1 (not optimized)
Hot side louver angle (°)	Θ_h	30	30	1 (not optimized)
Split plate thickness (mm)	t_{sp}	0.5	0.5	1 (not optimized)

Table B.2
Equations for the heat exchanger geometry.

Parameter	Equation
Liquid side geometry	
Tube depth	$T_d = F_d$
Tube pitch	$T_p = D_m + F_l$
Tube length	$T_l = \left(\frac{n_{fin,act}}{n_{tube}+1}\right)F_p$
Minor tube diameter	$D_{t,min} = D_m - 2T_t$
Mean tube diameter	$D_{t,mean} = (D_m + D_{t,min})/2$
Mean perimeter of tube cross section per tube	$P_{m,tube} = \pi D_{t,mean} + 2(T_d - 2T_t - D_{t,mean})$
Liquid side surface area	$A_{s,tube} = P_{m,tube} T_l n_{tube}$
Liquid side flow cross section per tube	$A_{cr,tube} = \frac{\pi (D_{t,min})^2}{4} + D_{t,min}(T_d - 2T_t - D_{t,min})$
Liquid side flow cross section	$A_{cr,liq} = A_{cr,tube} n_{tube}$
Liquid side hydraulic diameter	The hydraulic diameter is defined as $d_h = 4A_{cr}/P_{wetted}$ where A_{cr} is the cross section and P_{wetted} is the wetted perimeter of the tube [47,48]. In the case of a flat tube (Type "C" in refs. [49,50]), d_h is given by $d_h = \frac{4A_{cr,tube}}{\pi D_{t,min} + 2(T_d - 2T_t - D_{t,min})}$
Air side geometry	

(continued on next page)

Table B.2 (*continued*)

Parameter	Equation
Perimeter of fin secondary surface cross section per segment	$P_{\mathrm{fin,sgm}} = \pi\left(F_{\mathrm{p}} - F_{\mathrm{t}}\right) + 2\left(F_{\mathrm{l}} - F_{\mathrm{t}} - \left(F_{\mathrm{p}} - F_{\mathrm{t}}\right)\right)$
Wetted perimeter of gas side per segment	$P_{\mathrm{wet,gas,sgm}} = P_{\mathrm{fin,sgm}} + 2F_{\mathrm{p}}$
Fin surface area	$A_{\mathrm{fin}} = P_{\mathrm{fin,sgm}} F_{\mathrm{d}} n_{\mathrm{fin,act}}$
Gas side surface area	$A_{\mathrm{s,gas}} = P_{\mathrm{wet,gas,sgm}} F_{\mathrm{d}} n_{\mathrm{fin,act}}$
Gas side flow cross section per fin segment	$A_{\mathrm{cr,gas,sgm}} = F_{\mathrm{p}} F_{\mathrm{l}} - \frac{\pi\left(F_{\mathrm{p}} - F_{\mathrm{t}}\right)F_{\mathrm{t}}}{2} - \left(F_{\mathrm{l}} - \left(F_{\mathrm{p}} - F_{\mathrm{t}}\right)\right)F_{\mathrm{t}}$
Gas side flow cross section	$A_{\mathrm{cr,gas}} = n_{\mathrm{fin,act}} A_{\mathrm{cr,gas,sgm}}$
Gas side hydraulic diameter	$d_{\mathrm{h}} = \frac{4A_{\mathrm{cr,gas,sgm}}}{P_{\mathrm{wet,gas,sgm}}}$
Parameters for the air-to-liquid case	
Number of tubes	$n_{\mathrm{tube}} = \mathrm{ceil}\left(\sqrt{T_{\mathrm{p}} F_{\mathrm{p}} n_{\mathrm{fin}}} / T_{\mathrm{p}}\right) - 1$ The term -1 is included because both outer sides of the heat exchanger core are cold sides
Actual number of fin segments	$n_{\mathrm{fin,act}} = \mathrm{ceil}\left(\frac{n_{\mathrm{fin}}}{n_{\mathrm{tube}} + 1}\right)(n_{\mathrm{tube}} + 1)$
Gas side frontal area	$A_{\mathrm{hx,front}} = \left(n_{\mathrm{tube}} T_{\mathrm{p}} + F_{\mathrm{l}}\right) T_{\mathrm{l}}$
Mass per tube	$m_{\mathrm{tube}} = P_{\mathrm{m,tube}} t_{\mathrm{wall}} T_{\mathrm{l}} \rho_{\mathrm{Al}}$
Mass per fin segment	$m_{\mathrm{fin,sgm}} = \frac{P_{\mathrm{fin,sgm}}}{2} F_{\mathrm{t}} F_{\mathrm{d}} \rho_{\mathrm{Al}}$
Density of aluminum	$\rho_{\mathrm{Al}} = 2700\,\mathrm{kg/m^3}$
Heat exchanger mass	$m_{\mathrm{hx}} = m_{\mathrm{fin,sgm}} n_{\mathrm{fin,act}} + m_{\mathrm{tube}} n_{\mathrm{tube}}$
Heat exchanger outer volume	$V_{\mathrm{hx}} = A_{\mathrm{hx,front}} F_{\mathrm{d}}$
Parameters for the air-to-air case	
Equivalent tube pitch for cold air side	$T_{\mathrm{p,eq,c}} = F_{\mathrm{l,c}} + F_{\mathrm{l,h}} + 2t_{\mathrm{sp}}$
Equivalent tube pitch for hot air side	$T_{\mathrm{p,eq,h}} = F_{\mathrm{l,h}} + F_{\mathrm{l,c}} + 2t_{\mathrm{sp}}$
Equivalent tube major diameter for cold air side	$D_{\mathrm{m,eq,c}} = F_{\mathrm{l,h}} + 2t_{\mathrm{sp}}$
Equivalent tube major diameter for hot air side	$D_{\mathrm{m,eq,h}} = F_{\mathrm{l,c}} + 2t_{\mathrm{sp}}$
Number of cold side fin layers	$n_{\mathrm{l,c}} = \mathrm{ceil}\left(\sqrt{n_{\mathrm{fin,c}} F_{\mathrm{p,c}} T_{\mathrm{p,eq,c}}} / T_{\mathrm{p,eq,c}}\right) - 1$ The term -1 is included because the parameter $n_{\mathrm{l,c}}$ describes the number of full-size layers (there are $n_{\mathrm{l,c}}$-1 layers of fin length F_{l} and 2 outer layers with fin length $F_{\mathrm{l}}/2$).
Number of hot side fin layers	$n_{\mathrm{l,h}} = n_{\mathrm{l,c}}$
Number of split plates	$n_{\mathrm{sp}} = 2(n_{\mathrm{l,c}} + 1)$
Actual number of cold side fin segments	$n_{\mathrm{fin,act,c}} = \mathrm{ceil}(n_{\mathrm{fin,c}}/n_{\mathrm{l,c}}) \cdot n_{\mathrm{l,c}}$ The two half-size fin segments at the ends of the core are considered as one full-size fin segment.
Actual number of hot side fin segments	$n_{\mathrm{fin,act,h}} = \mathrm{ceil}(n_{\mathrm{fin,h}}/n_{\mathrm{l,h}}) \cdot n_{\mathrm{l,h}}$
Cold side fin depth	$F_{\mathrm{d,c}} = \left(\frac{n_{\mathrm{fin,act,h}}}{n_{\mathrm{l,h}}}\right) F_{\mathrm{p,h}}$
Hot side fin depth	$F_{\mathrm{d,h}} = \left(\frac{n_{\mathrm{fin,act,c}}}{n_{\mathrm{l,c}}}\right) F_{\mathrm{p,c}}$
Cold side frontal area	$A_{\mathrm{hx,front}} = n_{\mathrm{fin,act,c}} F_{\mathrm{p,c}} T_{\mathrm{p,eq,c}}$
Mass per cold side fin segment	$m_{\mathrm{fin,sgm,c}} = \frac{P_{\mathrm{fin,sgm,c}}}{2} F_{\mathrm{t,c}} F_{\mathrm{d,c}} \rho_{\mathrm{Al}}$
Mass per hot side fin segment	$m_{\mathrm{fin,sgm,h}} = \frac{P_{\mathrm{fin,sgm,h}}}{2} F_{\mathrm{t,h}} F_{\mathrm{d,h}} \rho_{\mathrm{Al}}$
Mass per split plate	$m_{\mathrm{sp}} = F_{\mathrm{d,c}} F_{\mathrm{d,h}} t_{\mathrm{sp}} \rho_{\mathrm{Al}}$
Density of aluminum	$\rho_{\mathrm{Al}} = 2700\,\mathrm{kg/m^3}$
Heat exchanger mass	$m_{\mathrm{hx}} = m_{\mathrm{fin,sgm,c}} n_{\mathrm{fin,act,c}} + m_{\mathrm{fin,sgm,h}} n_{\mathrm{fin,act,h}} + m_{\mathrm{sp}} n_{\mathrm{sp}}$
Heat exchanger outer volume	$V_{\mathrm{hx}} = F_{\mathrm{d,c}} F_{\mathrm{d,h}} (n_{\mathrm{l,c}} F_{\mathrm{l,c}} + n_{\mathrm{l,h}} F_{\mathrm{l,h}} + n_{\mathrm{sp}} t_{\mathrm{sp}})$

Appendix C. Compressor model details

This appendix describes the analytic expressions and parameter fit procedure for the Jensen-Kristensen sub-model. The expression for the reduced rotational speed is given by Eqs. (C.1) to (C.6) [55,56].

$$\Pi_{\mathrm{cp}} = \left(\frac{\Psi U_{\mathrm{c}}^2}{2c_{\mathrm{p,air}} T_{\mathrm{cp,in}}} + 1\right)^{\frac{\gamma}{\gamma - 1}} \tag{C.1}$$

$$U_{\mathrm{c}} = \pi d_{\mathrm{c}} n_{\mathrm{cp,red}} \tag{C.2}$$

U_{c} is the blade tip speed, d_{c} the outer diameter of the impeller and γ the heat capacity ratio. The dimensionless head parameter Ψ is given by [55,56]

$$\Psi = \frac{k_{n,1} + k_{n,2}\Phi}{k_{n,3} - \Phi} \tag{C.3}$$

$$\Phi = \frac{\dot{m}_{\mathrm{cp,red}} R_{\mathrm{sp,air}} T_{\mathrm{cp,in}}}{p_{\mathrm{cp,in}} \frac{\pi}{4} d_{\mathrm{c}}^2 U_{\mathrm{c}}} \tag{C.4}$$

$$k_{n,i} = k_{n,ij} + k_{n,ij} Ma_{\mathrm{cp}} \quad \text{for } i = 1, 2, 3 \text{ and } j = 1, 2 \tag{C.5}$$

$$Ma_{\mathrm{cp}} = \frac{U_{\mathrm{c}}}{\sqrt{\gamma R_{\mathrm{sp,air}} T_{\mathrm{cp,in}}}} \tag{C.6}$$

where Φ is the normalized compressor flow rate, Ma_{cp} the Mach number and $k_{n,ij}$ are fitted coefficients. The analytic expression for isentropic efficiency is [55,56]

$$\eta_{cp,s} = k_{e,1}\Phi^2 + k_{e,2}\Phi + k_{e,3} \tag{C.7}$$

$$k_{e,i} = \frac{k_{e,ij} + k_{e,ij}Ma_{cp}}{k_{e,ij} - Ma_{cp}} \quad \text{for } i = 1,2,3 \text{ and } j = 1,2,3 \tag{C.8}$$

where $k_{e,ij}$ are fitted coefficients. The parameters $k_{n,ij}$ and the impeller diameter d_c are fitted to 110 discrete points ($\dot{m}_{cp,red}$, Π_{cp}, $n_{cp,red}$) from the rotational speed map of a Rotrex C38-91 compressor [25]. This is done by minimizing the difference between the calculated rotational speed map and the manufacturer datapoints with MATLAB's Levenberg-Marquardt optimization algorithm. Analogously, the parameters $k_{e,ij}$ are fitted to 565 discrete points ($\dot{m}_{cp,red}$, Π_{cp}, $\eta_{cp,s}$) from the compressor's efficiency map [25]. The datapoints that are used to fit these coefficients are shown in Fig. C.1 (a) and (c), the corresponding result of the semi-empirical model is shown in Fig. C.1 (b) and (d). The datapoints were obtained from the public manufacturer datasheet with the open-source software WebPlotDigitizer.

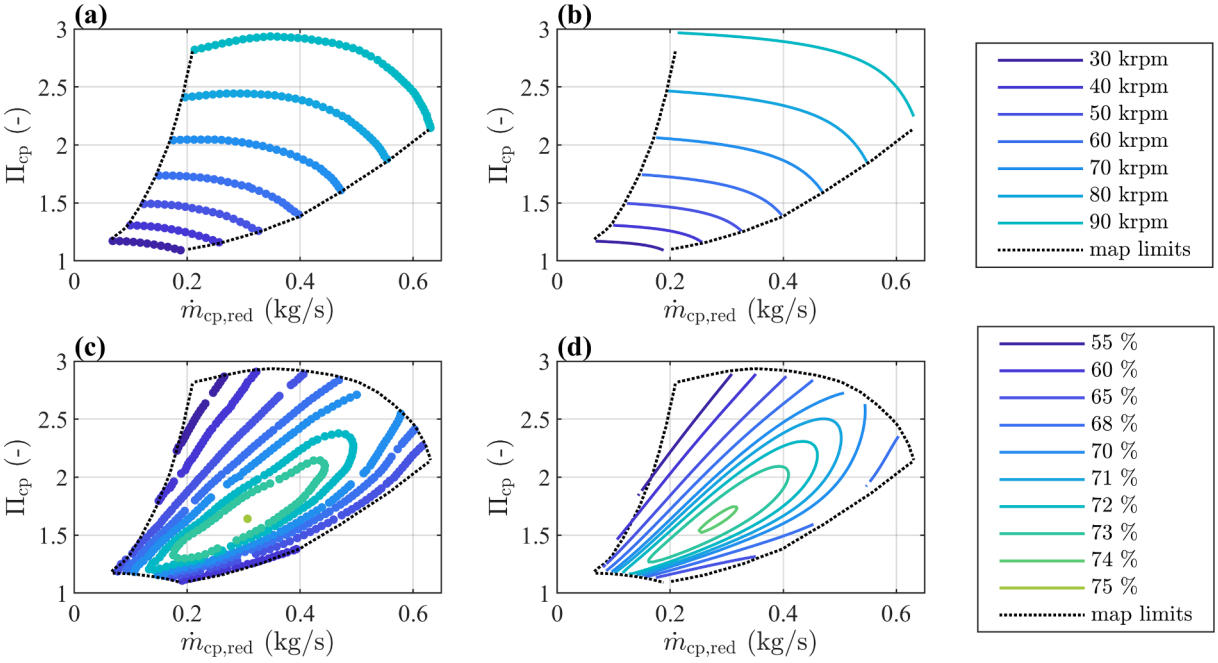

Fig. C.1. Rotational speed and efficiency map of a Rotrex C38-91 compressor. (a) Rotational speed map, manufacturer data [25] (b) rotational speed map based on semi-empirical model (c) Efficiency map, manufacturer data [25] (d) efficiency map based on semi-empirical model.

Appendix D. Additional component models

The power consumption of the coolant pump is given by [78]

$$P_{pu} = \frac{(\Delta p_{hx,FC,h} + \Delta p_{stack,cw})\dot{m}_{stack,cw}}{\rho_{cw}\eta_{pu,eh}\eta_{pu,pc}} \tag{D.1}$$

and the parameters in Table D.1. The losses in the pump are attributed to an increase in coolant temperature ΔT_{pu}.

$$\dot{Q}_{pu} = \frac{(\Delta p_{hx,FC,h} + \Delta p_{stack,cw})\dot{m}_{stack,cw}}{\rho_{cw}}\left(\frac{1}{\eta_{pu,eh}} - 1\right) \tag{D.2}$$

$$\Delta T_{pu} = \frac{\dot{Q}_{pu}}{\dot{m}_{stack,cw}c_{p,cw}} \tag{D.3}$$

The density $\rho_{cw}(T)$ and heat capacity $c_{p,cw}(T)$ of the coolant are evaluated at the known temperature at the stack's coolant inlet. The pump's mass and volume are determined by linearly scaling the properties of a baseline design (see Table D.1).

$$m_{pu} = m_{pu,base}\frac{\dot{m}_{pu}}{\dot{m}_{pu,base}} \tag{D.4}$$

$$V_{pu} = V_{pu,base}\frac{\dot{m}_{pu}}{\dot{m}_{pu,base}} \tag{D.5}$$

The power consumption of the anode recirculation blower is given by [79]

$$P_{ar} = \frac{\Delta p_{stack,A} \dot{m}_{ar}}{\rho_{ar} \eta_{ar,h} \eta_{ar,em} \eta_{ar,pc}} \tag{D.6}$$

and the parameters in Table D.1. The recirculated mass flow is given by

$$\dot{m}_{ar} = \frac{i A_{cell} N_{cell} M_{H2}}{2F} (\lambda_{H2,int} - \lambda_{H2}) \left(\frac{1}{w_{H2}} \right) \tag{D.7}$$

where $\lambda_{H2} = 1.05$ is the overall stoichiometric ratio (based on hydrogen flow that is added to the recirculation loop) and $\lambda_{H2,int} = 2$ is the internal stoichiometric ratio (based on hydrogen flow that enters the cells). The density of the recirculated fluid ρ_{ar} and the mass fraction of hydrogen in the recirculation loop w_{H2} are known from the stack model. The pressure drop in the stack's anode channels

$$\Delta p_{stack,A} = k_{pC} \frac{\dot{m}_{stack,A,in}}{N_{cell}} \tag{D.8}$$

is calculated with the same coefficient k_{pC} as for the cathode side (see section 3.1.2). The waste heat $\dot{Q}_{ar}$ due to the non-ideal blower is removed by the stack cooling loop.

$$\dot{Q}_{ar} = P_{ar} \eta_{ar,em} \eta_{ar,pc} (1 - \eta_{ar,h}) \tag{D.9}$$

The remaining losses in the motor and power converter are removed via convective heat transfer to the surroundings. The blower's mass and volume are determined by linearly scaling the mass and volume of a baseline design (see Table D.1).

$$m_{ar} = m_{ar,base} \frac{\dot{m}_{ar}}{\dot{m}_{ar,base}} \tag{D.10}$$

$$V_{ar} = V_{ar,base} \frac{\dot{m}_{ar}}{\dot{m}_{ar,base}} \tag{D.11}$$

Table D.1
Component model parameters. Coolant pump parameters are estimated based on an aircraft-rated fuel pump (Double Ended Fuel Booster Pump Type 7100, Eaton Aerospace). Anode recirculation blower parameters are estimated based on manufacturer data (G-BH100 side channel vacuum pump/compressor, Gardner Denver).

Parameter	Symbol	Value	Background
Coolant pump			
Coolant pump efficiency (including electric motor) (-)	$\eta_{pu,eh}$	0.47	Manufacturer data
Power converter efficiency (stack to DC bus)	$\eta_{DC/DC}$	0.97	[54], for high powers
Power converter efficiency (DC bus to electric motor)	$\eta_{DC/AC}$	0.80	[54], for low powers
Overall power converter efficiency	$\eta_{pu,pc}$	0.78	
Rated mass flow of baseline pump design (kg/s)	$\dot{m}_{pu,base}$	5.0	Manufacturer data
Mass of baseline pump design (kg)	$m_{pu,base}$	3.4	Manufacturer data
Volume of baseline pump design (m^3)	$V_{pu,base}$	0.0077	Manufacturer data
Anode recirculation blower			
Blower efficiency (mechanic to hydraulic) as defined in ref. [79] (-)	$\eta_{ar,mh}$	0.3	[79]
Blower efficiency (electric to mechanic), (-)	$\eta_{ar,em}$	0.8	[79]
Power converter efficiency (stack to DC bus)	$\eta_{DC/DC}$	0.97	[54], for high powers
Power converter efficiency (DC bus to electric motor)	$\eta_{DC/AC}$	0.80	[54], for low powers
Overall power converter efficiency	$\eta_{ar,pc}$	0.78	
Overall anode stoichiometric ratio (-)	λ_{H2}	1.05	Estimated based on stack test bench
Internal anode stoichiometric ratio (-)	$\lambda_{H2,int}$	2.0	Estimated based on stack test bench
Rated mass flow of baseline blower design (kg/s)	$\dot{m}_{ar,base}$	0.003	Manufacturer data
Mass of baseline blower design (kg)	$m_{ar,base}$	1.2	Manufacturer data
Volume of baseline blower design (m^3)	$V_{ar,base}$	$9.38 \cdot 10^{-4}$	Manufacturer data

Appendix E. System simulation flow chart

The interaction of the component models during the simulation of the overall system is shown in Fig. E.1. The flow chart visualizes the computation during the step "Simulate fully sized system" in stages 3 and 4 of Fig. 3 in more detail. As described in section 4.3, that step is repeated for each flight phase and each investigated combination of the stack's cathode inlet pressure $p_{stack,C,in}$ and relative humidity $RH_{stack,C,in}$. The compressor's pressure ratio and the stack's current density are determined with MATLAB's non-linear equation solver *fminsearch*.

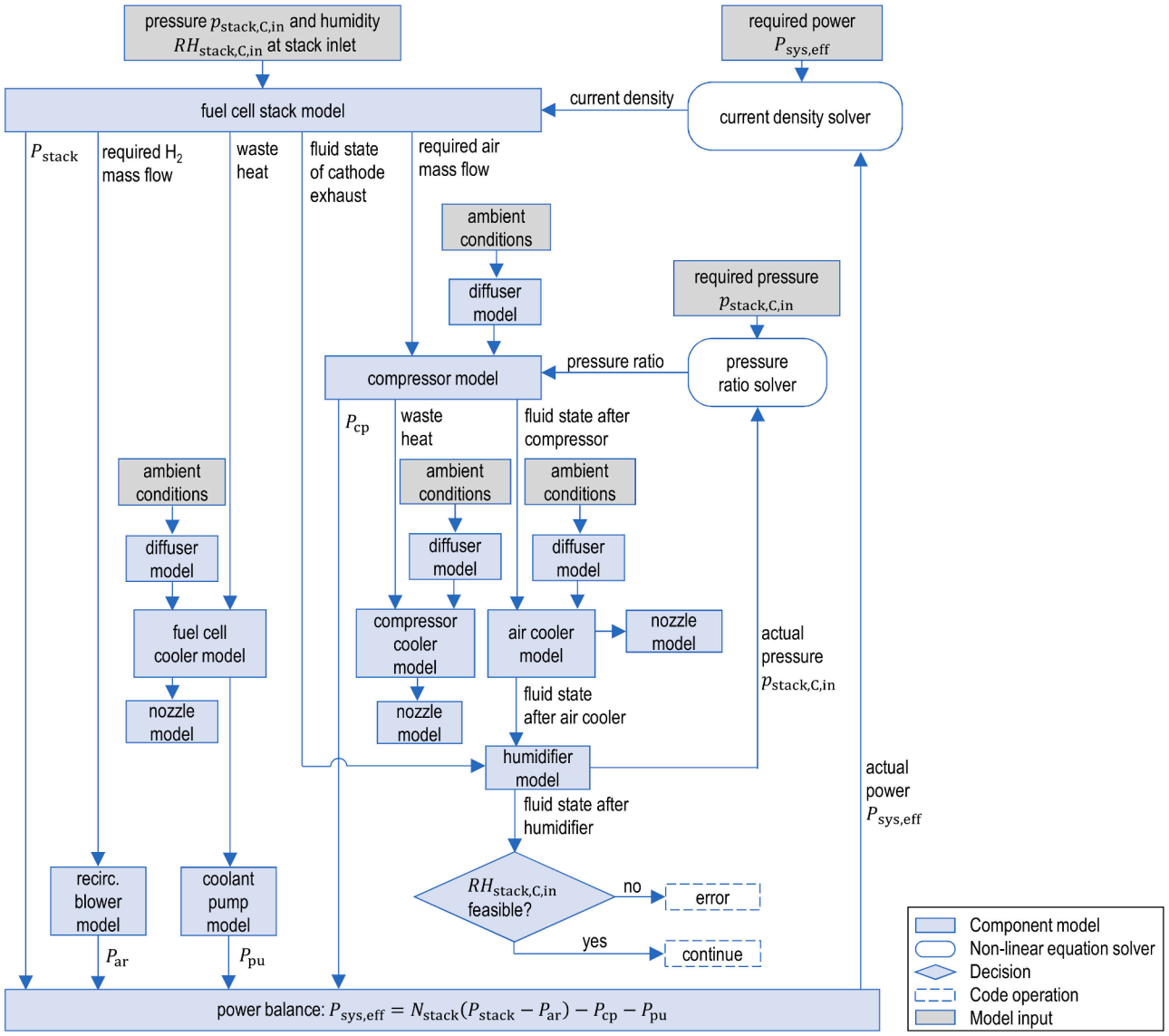

Fig. E.1. Flow chart for the interaction of the component models during the overall system simulation. The power flows P_{stack}, P_{cp}, P_{pu} and P_{ar} are defined in section 2.1.

References

[1] Klöwer M, Allen MR, Lee DS, Proud SR, Gallagher L, Skowron A. Quantifying aviation's contribution to global warming. Environ Res Lett 2021;16(10):104027. https://doi.org/10.1088/1748-9326/ac286e.

[2] Adler EJ, Martins JRRA. Hydrogen-powered aircraft: fundamental concepts, key technologies, and environmental impacts. Prog Aerosp Sci 2023;141:100922. https://doi.org/10.1016/j.paerosci.2023.100922.

[3] Massaro MC, Biga R, Kolisnichenko A, Marocco P, Monteverde AHA, Santarelli M. Potential and technical challenges of on-board hydrogen storage technologies coupled with fuel cell systems for aircraft electrification. J Power Sources 2023; 555:232397. https://doi.org/10.1016/j.jpowsour.2022.232397.

[4] Hoelzen J, Silberhorn D, Zill T, Bensmann B, Hanke-Rauschenbach R. Hydrogen-powered aviation and its reliance on green hydrogen infrastructure – review and research gaps. Int J Hydrogen Energy 2022;47(5):3108–30. https://doi.org/10.1016/j.ijhydene.2021.10.239.

[5] Universal Hydrogen Co. *Press release: Universal Hydrogen Successfully Completes First Flight of Hydrogen Regional Airliner*. 2023. https://hydrogen.aero/press-releases/universal-hydrogen-successfully-completes-first-flight-of-hydrogen-regional-airliner/ (accessed July 14, 2023).

[6] Airbus SE. *Press release: Airbus to trial in-flight auxiliary power entirely generated by hydrogen*. 2023. https://www.airbus.com/en/newsroom/press-releases/2023-06-airbus-to-trial-in-flight-auxiliary-power-entirely-generated-by (accessed July 14, 2023).

[7] Abu Kasim AFB, Chan MSC, Marek EJ. Performance and failure analysis of a retrofitted Cessna aircraft with a fuel cell power system fuelled with liquid hydrogen. J Power Sources 2022;521:230987. https://doi.org/10.1016/j.jpowsour.2022.230987.

[8] Epstein AH. Aeropropulsion for Commercial Aviation in the Twenty-First Century and Research Directions Needed. AIAA J 2014;52(5):901–11. https://doi.org/10.2514/1.J052713.

[9] Smith JR, Mastorakos E. An energy systems model of large commercial liquid hydrogen aircraft in a low-carbon future. Int J Hydrogen Energy 2023. https://doi.org/10.1016/j.ijhydene.2023.04.039.

[10] Kösters TL, Liu X, Kožulović D, Wang S, Friedrichs J, Gao X. Comparison of phase-change-heat-pump cooling and liquid cooling for PEM fuel cells for MW-level aviation propulsion. Int J Hydrogen Energy 2022;47(68):29399–412. https://doi.org/10.1016/j.ijhydene.2022.06.235.

[11] Sparano M, Sorrentino M, Troiano G, Cerino G, Piscopo G, Basaglia M, et al. The future technological potential of hydrogen fuel cell systems for aviation and preliminary co-design of a hybrid regional aircraft powertrain through a mathematical tool. Energ Conver Manage 2023;281:116822. https://doi.org/10.1016/j.enconman.2023.116822.

[12] Yang Z, Du Q, Jia Z, Yang C, Xuan J, Jiao K. A comprehensive proton exchange membrane fuel cell system model integrating various auxiliary subsystems. Appl Energy 2019;256:113959. https://doi.org/10.1016/j.apenergy.2019.113959.

[13] Park J, Lee D, Lim D, Yee K. A refined sizing method of fuel cell-battery hybrid system for eVTOL aircraft. Appl Energy 2022;328:120160. https://doi.org/10.1016/j.apenergy.2022.120160.

[14] Vietze M, Weiland S. System analysis and requirements derivation of a hydrogen-electric aircraft powertrain. Int J Hydrogen Energy 2022;47(91):38793–810. https://doi.org/10.1016/j.ijhydene.2022.09.052.

[15] Li Y, Hu Z, Liu H, Xu L, Li J, Xu L, et al. Comprehensive analysis of cathode air pressure of fuel cell powertrain system of aircraft: performance, efficiency, and control. Energ Conver Manage 2023;283:116903. https://doi.org/10.1016/j.enconman.2023.116903.

[16] Lüdders HP, Strummel H, Thielecke F. Model-based development of multifunctional fuel cell systems for more-electric-aircraft. CEAS Aeronaut J 2013; 4(2):151–74. https://doi.org/10.1007/s13272-013-0062-3.

[17] Schröder M, Becker F, Kallo J, Gentner C. Optimal operating conditions of PEM fuel cells in commercial aircraft. Int J Hydrogen Energy 2021;46(66):33218–40. https://doi.org/10.1016/j.ijhydene.2021.07.099.

[18] G. Atanasov, "Comparison of Sustainable Regional Aircraft Concepts," presented at Deutscher Luft- und Raumfahrtkongress (conference), Dresden, Germany, 2022.

[19] Avions de Transport Régional GIE. *ATR72-600*. https://www.atr-aircraft.com/our-aircraft/atr-72-600/ (accessed Nov 28, 2023).

[20] Gohardani AS, Doulgeris G, Singh R. Challenges of future aircraft propulsion: a review of distributed propulsion technology and its potential application for the all electric commercial aircraft. Prog Aerosp Sci 2011;47(5):369–91. https://doi.org/10.1016/j.paerosci.2010.09.001.

[21] Powercell Sweden AB. *Datasheet Powercell P Stack*. https://powercellgroup.com/wp-content/uploads/2023/10/p-stack-v-222.pdf (accessed Feb 21, 2024).

[22] M. Sinnett. *Boeing: 787 No-Bleed Systems: Saving Fuel and enhancing operational efficiencies*. 2007. https://www.boeing.com/commercial/aeromagazine/articles/qtr_4_07/AERO_Q407_article2.pdf (accessed Mar 03, 2021).

[23] S. Campanari, G. Manzolini, A. Beretti, and U. Wollrab, Performance Assessment of Turbocharged Pem Fuel Cell Systems for Civil Aircraft Onboard Power Production, *Journal of Engineering for Gas Turbines and Power,* vol. 130, no. 2, 2008, doi: 10.1115/1.2772636.

[24] Dakshina Murty V. Turbomachinery: concepts, applications, and design. Milton, United Kingdom: Taylor & Francis Group; 2018.

[25] Rotrex A/S. *Rotrex C-range C38 supercharger*. https://www.rotrexshop.com/wp-content/uploads/2021/12/Rotrex_Technical_Datasheet_C38_Rev6.0.pdf (accessed Feb 21, 2024).

[26] Feneley AJ, Pesiridis A, Andwari AM. Variable geometry Turbocharger Technologies for Exhaust Energy Recovery and Boosting-a Review. Renew Sustain Energy Rev 2017;71:959–75. https://doi.org/10.1016/j.rser.2016.12.125.

[27] Kim DK, Min HE, Kong IM, Lee MK, Lee CH, Kim MS, et al. Parametric study on interaction of blower and back pressure control valve for a 80-kW class PEM fuel cell vehicle. Int J Hydrogen Energy 2016;41(39):17595–615. https://doi.org/10.1016/j.ijhydene.2016.07.218.

[28] Burschyk T, Silberhorn D, Wehrspohn J, Kühlen M, Zill T. Scenario-based implications of liquid hydrogen storage tank insulation quality for a short-range aircraft concept. In: presented at AIAA AVIATION 2023 Forum; 2023. https://doi.org/10.2514/6.2023-3522.

[29] E. W. Lemmon, M. O. McLinden, and D. G. Friend, "Thermophysical Properties of Fluid Systems," in *NIST Chemistry WebBook, NIST Standard Reference Database Number 69*, P. J. Linstrom and W. G. Mallard Eds. Gaithersburg MD: National Institute of Standards and Technology.

[30] BASF SE. *Physical properties of GLYSANTIN® coolants*. https://www.glysantin.de/sites/default/files/2019-06/GLYSANTIN%C2%AE%20Graphs.pdf (accessed Jan 03, 2023).

[31] D. Kondepudi and I. Prigogine, "Modern Thermodynamics: From Heat Engines to Dissipative Structures ". Chichester, UK: John Wiley & Sons, Ltd, 2014, ch. Basic Thermodynamics of Gases, Liquids and Solids.

[32] Torenbeek E. "Appendix B: international Standard atmosphere," in *Advanced aircraft design*. Chichester, United Kingdom: John Wiley and Sons Ltd; 2013. p. 397–8.

[33] European Union Aviation Safety Agency (EASA), "CS-25 Certification Specifications and Acceptable Means of Compliance for Large Aeroplanes. Amendment 24, section CS-25.1043," 2020.

[34] Affonso Nóbrega PH. A review of physics-based low-temperature proton-exchange membrane fuel cell models for system-level water and thermal management studies. J Power Sources 2023;558:232585. https://doi.org/10.1016/j.jpowsour.2022.232585.

[35] Montaner Ríos G, Schirmer J, Gentner C, Kallo J. Efficient thermal management strategies for cold starts of a proton exchange membrane fuel cell system. Appl Energy 2020;279:115813. https://doi.org/10.1016/j.apenergy.2020.115813.

[36] Weber AZ, Newman J. Transport in Polymer-electrolyte membranes: II. mathematical model. J Electrochem Soc 2004;151(2):A311. https://doi.org/10.1149/1.1639157.

[37] Vetter R, Schumacher JO. Free open reference implementation of a two-phase PEM fuel cell model. Comput Phys Commun 2019;234:223–34. https://doi.org/10.1016/j.cpc.2018.07.023.

[38] Goshtasbi A, Pence BL, Chen J, DeBolt MA, Wang C, Waldecker JR, Hirano S, Ersal T. A mathematical model toward real-time monitoring of automotive PEM fuel cells. J Electrochem Soc 2020;vol. 167(2).

[39] Fumatech BWT GmbH. *Membrane Humidifiers*. 2020. https://www.fumatech.com/NR/rdonlyres/0B9A1C7F-5BA6-4409-A003-5C4E79CD61AB/0/FUMATECH_BWT_GmbHMembrane_Humidifiers.pdf (accessed Mar 03, 2021).

[40] Cave P, Mérida W. Water flux in membrane fuel cell humidifiers: flow rate and channel location effects. J Power Sources 2008;175(1):408–18. https://doi.org/10.1016/j.jpowsour.2007.08.103.

[41] Huang J. A simple accurate formula for calculating saturation vapor pressure of water and ice. J Appl Meteorol Climatol 2018;57(6):1265–72. https://doi.org/10.1175/JAMC-D-17-0334.1.

[42] Koester S, Roghmans F, Wessling M. Water vapor permeance: the interplay of feed and permeate activity. J Membr Sci 2015;485:69–78. https://doi.org/10.1016/j.memsci.2015.03.019.

[43] Fumatech BWT GmbH. *Ecomate H50N-FL datasheet*. 2022. https://www.bwt.com/en/-/media/bwt/fumatech/datasheets/new/ecomate/h50n-fl.pdf?rev=f43c7291a8584e47ba86d3e06af28c16 (accessed Feb 21, 2023).

[44] J. Tallgren and J. Ihonen. *Deliverable 3.1. MARANDA, H2020 FCH JU project no. 735717*. 2018. https://ec.europa.eu/research/participants/documents/downloadPublic?documentIds=080166e5be1c8dbb&appId=PPGMS (accessed Jun 15, 2022).

[45] Fumatech BWT GmbH. *Ecomate H20N datasheet*. 2022. https://www.bwt.com/en/-/media/bwt/fumatech/datasheets/new/ecomate/h20n.pdf?rev=b99460b8bec5415e9eca2194e6ba6183 (accessed Feb 21, 2023).

[46] Cahalan T, Rehfeldt S, Bauer M, Becker M, Klein H. Analysis of membranes used in external membrane humidification of PEM fuel cells. Int J Hydrogen Energy 2017; 42(22):15370–84. https://doi.org/10.1016/j.ijhydene.2017.03.215.

[47] J. E. Hesselgreaves, R. Law, and D. A. Reay, *Compact Heat Exchangers, 2nd Edition. Selection, Design and Operation.* Amsterdam: Elsevier Ltd., 2016.

[48] Baehr HD, Stephan K. Heat and mass transfer. 1st ed. Berlin, Heidelberg: Springer; 2013.

[49] Chang Y-J, Wang C-C. A generalized heat transfer correlation for iouver fin geometry. Int J Heat Mass Transf 1997;40(3):533–44. https://doi.org/10.1016/0017-9310(96)00116-0.

[50] Chang Y-J, Chang W-J, Li M-C, Wang C-C. An amendment of the generalized friction correlation for louver fin geometry. Int J Heat Mass Transf 2006;49(21): 4250–3. https://doi.org/10.1016/j.ijheatmasstransfer.2006.05.011.

[51] Struchtrup H. Thermodynamics and energy conversion. 1st ed. Berlin Heidelberg: Springer-Verlag; 2014.

[52] Rotrex A/S. *Rotrex EK40 Fuel Cell Compressor*. https://rotrex-fuel-cell-compressor.com/wp-content/uploads/2022/05/Rotrex-Technical-Datasheet-EK40-Rev1.2.pdf (accessed Jul 28, 2022).

[53] Rotrex A/S. *Rotrex C-range C38R supercharger*. https://www.rotrexshop.com/wp-content/uploads/2021/12/Rotrex_Technical_Datasheet_C38R_Rev2.0.pdf (accessed Feb 21, 2024).

[54] Mecrow BC, Jack AG. Efficiency trends in electric machines and drives. Energy Policy 2008;36(12):4336–41. https://doi.org/10.1016/j.enpol.2008.09.042.

[55] Jensen J-P, Kristensen AF, Sorenson SC, Houbak N. "Mean Value Modeling of a Small Turbocharged Diesel Engine" 1991. https://doi.org/10.4271/910070.

[56] P. Moraal and I. Kolmanovsky, Turbocharger Modeling for Automotive Control Applications, *SAE Technical Paper,* 1999, doi: 10.4271/1999-01-0908.

[57] Schröter J, Frank D, Radke V, Bauer C, Kallo J, Willich C. Influence of low inlet pressure and temperature on the compressor map limits of electrical turbo chargers for airborne fuel cell applications. Energies 2022;15(8). https://doi.org/10.3390/en15082896.

[58] Botros KK, Henderson JF. Developments in centrifugal compressor surge control: a technology assessment. presented at ASME 1993 International Gas Turbine and Aeroengine Congress and Exposition. 1993.

[59] Mann+Hummel GmbH. *Datasheet WaterPro water separator*. https://shop.mann-hummel.com/en/e-mobility/waterpro.html (accessed Feb 09, 2024).

[60] Vargas JVC, Bejan A. Thermodynamic optimization of finned crossflow heat exchangers for aircraft environmental control systems. Int J Heat Fluid Flow 2001; 22(6):657–65. https://doi.org/10.1016/S0142-727X(01)00129-1.

[61] German Aerospace Center (DLR). *Press release: Zero-emission air transport—first flight of four-seat passenger aircraft*. 2016. https://www.dlr.de/en/latest/news/2016/20160929_zero-emission-air-transport-first-flight-of-four-seat-passenger-aircraft-hy4_19469 (accessed July 21, 2023).

[62] Balli O, Hepbasli A. Energetic and exergetic analyses of T56 turboprop engine. Energ Conver Manage 2013;73:106–20. https://doi.org/10.1016/j.enconman.2013.04.014.

[63] Franck-Lacaze L, Bonnet C, Choi E, Moss J, Pontvianne S, Poirot H, et al. Ageing of PEMFC's due to operation at low current density: investigation of oxidative degradation. Int J Hydrogen Energy 2010;35(19):10472–81. https://doi.org/10.1016/j.ijhydene.2010.07.180.

[64] Powercell Sweden AB. *P System 100*. https://powercellgroup.com/segments/aviation/ (accessed Feb 23, 2024).

[65] Plug Power Inc. *Plug ProGen Fuel Cells for E-Mobility*. https://resources.plugpower.com/ecosystem-use-hydrogen/plug-progen-fuel-cells-for-e-mobility-english-2 (accessed Feb 12, 2024).

[66] Nuvera Fuel Cells LLC. *Nuvera E-Series Fuel Cell Engines*. https://www.nuvera.com/wp-content/uploads/2023/01/Nuvera-E-Series-Cutsheet_2023.pdf (accessed Feb 12, 2024).

[67] Pratt & Whitney. *PW100/150 Engines*. https://www.prattwhitney.com/en/products/regional-aviation-engines/pw100-150/ (accessed July 24, 2023).

[68] Clean Hydrogen Joint Undertaking. *Strategic Research and Innovation Agenda 2021-2027 - Annex 4*. 2022. https://www.clean-hydrogen.europa.eu/about-us/key-documents/strategic-research-and-innovation-agenda_en (accessed Feb 12, 2024).

[69] W. Bhatti, W. Wu, F. Doyle, J. Llambrich, H. Webber, and N. Town. *FlyZero Fuel Cells Roadmap Report FZO-PPN-COM-0033*. 2022. https://www.ati.org.uk/wp-content/uploads/2022/03/FZO-PPN-MAP-0032-Fuel-Cells-Roadmap.pdf (accessed Feb 12, 2024).

[70] Jinnouchi R, Kudo K, Kodama K, Kitano N, Suzuki T, Minami S, et al. The role of oxygen-permeable ionomer for polymer electrolyte fuel cells. Nat Commun 2021; 12(1):4956. https://doi.org/10.1038/s41467-021-25301-3.

[71] Zhang X, Haran KS. "High-specific-power electric machines for electrified transportation applications-technology options". In: IEEE Energy Conversion Congress and Exposition (ECCE), 18–22(2016) Sept. 2016; 2016. p. 1–8.
[72] O'Hayre R, Cha S-W, Colella W, Prinz FB. Fuel cell fundamentals. 3rd ed. Hoboken: John Wiley & Sons Inc; 2016.
[73] Zohuri B. Heat exchanger types and classifications. Compact Heat Exchangers. 1st ed. Cham: Springer; 2017.
[74] Weber AZ. Improved modeling and understanding of diffusion-media wettability on polymer-electrolyte-fuel-cell performance. J Power Sources 2010;195(16): 5292–304. https://doi.org/10.1016/j.jpowsour.2010.03.011.
[75] Goshtasbi A, Pence BL, Ersal T. Computationally efficient pseudo-2D non-isothermal modeling of Polymer electrolyte membrane fuel cells with two-phase phenomena. J Electrochem Soc 2016;163(13):F1412–32. https://doi.org/10.1149/2.0871613jes.
[76] Gostick JT, Ioannidis MA, Fowler MW, Pritzker MD. Wettability and capillary behavior of fibrous gas diffusion media for polymer electrolyte membrane fuel cells. J Power Sources 2009;194(1):433–44. https://doi.org/10.1016/j.jpowsour.2009.04.052.
[77] Weber AZ. Effective diffusion-medium thickness for simplified polymer-electrolyte-fuel-cell modeling. Electrochim Acta 2008;54(2):311–5. https://doi.org/10.1016/j.electacta.2008.07.084.
[78] Sulzer Pumps. Centrifugal pump handbook. Oxford, United Kingdom: Elsevier Science & Technology; 2010.
[79] Badami M, Mura M. Leakage effects on the performance characteristics of a regenerative blower for the hydrogen recirculation of a PEM fuel cell. Energ Conver Manage 2012;55:20–5. https://doi.org/10.1016/j.enconman.2011.10.002.